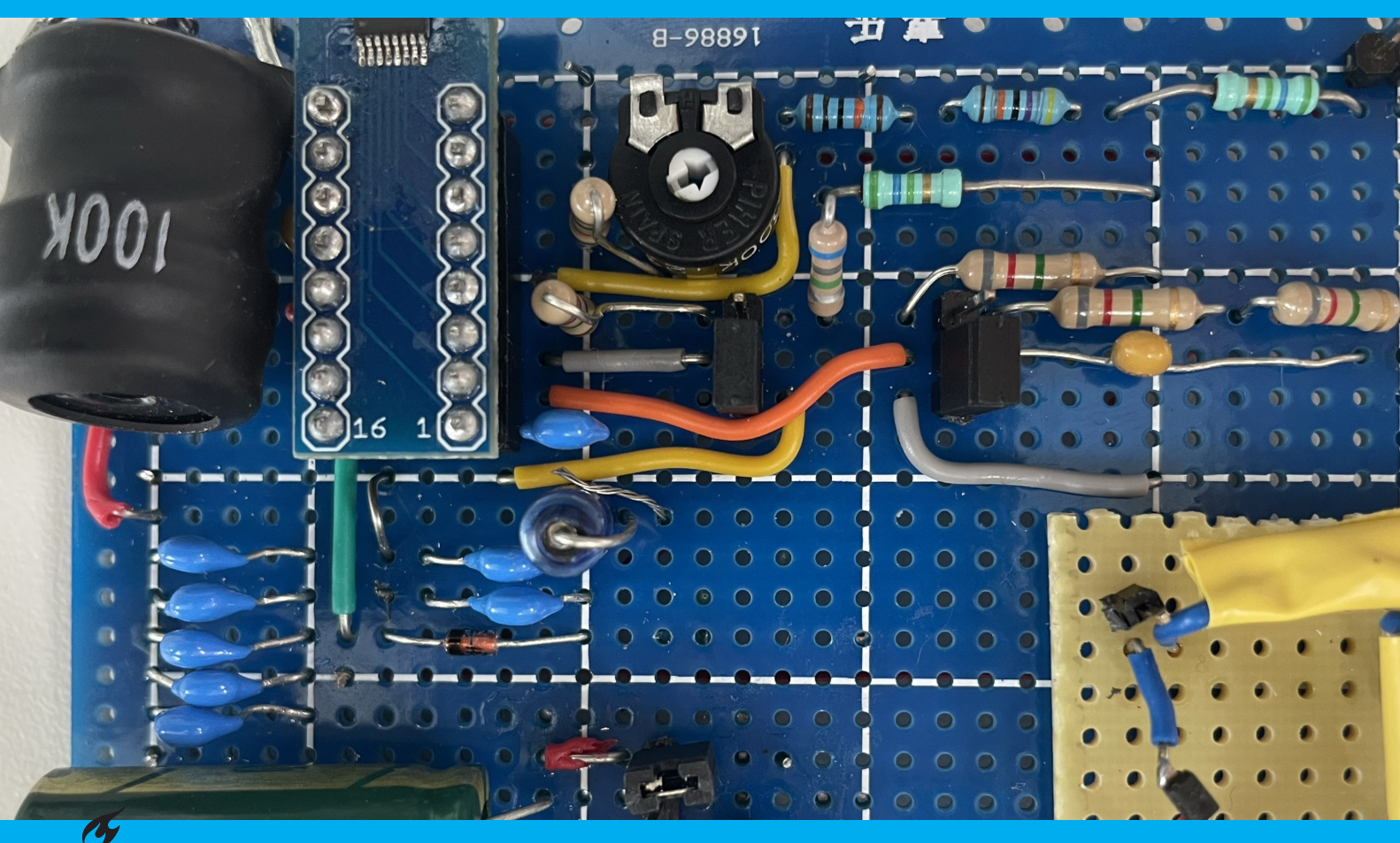
A Batteryless Inductive Energy Harvesting System

Rolando Russel & Waris Ibrahimi

In collaboration with

BSc Electrical Engineering EE3L11





A Batteryless Inductive Energy

Harvesting System

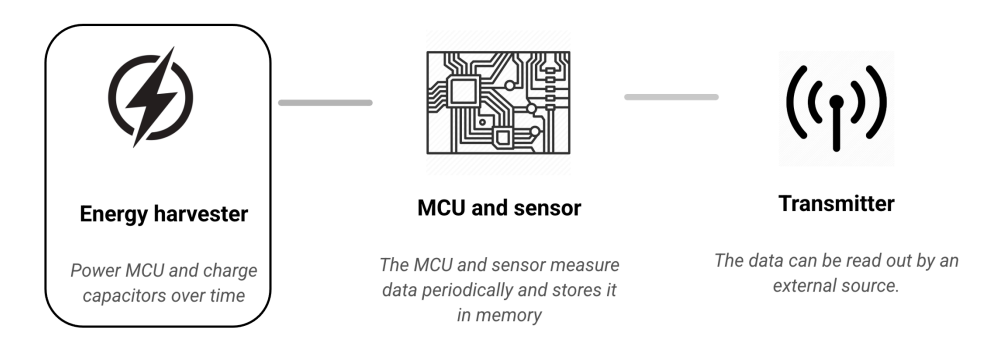
by

Rolando Russel & Waris Ibrahimi



Preface

As part of the TU Delft Bachelor Graduation Project, this thesis details the design and development of a wireless energy harvesting system, enabling a battery-free wireless temperature-sensing data logger.



Special thanks to our BAP supervisors, Dr. Kofi Makinwa and Dr. Suijin Du, for their invaluable guidance throughout this project. We also extend our gratitude to PhD researchers Floris van Mourik and Teije Onstein for their daily guidance and support. In addition, we sincerely thank Martin Schumacher and Dr. Chris Verhoeven for their assistance with component sourcing tasks. Finally, we greatly appreciate the contributions and collaboration of our colleagues: Kjell de Wit, Alec Reunis, Brian Joemmankhan and Stoyan Dinev.

Abstract

This thesis presents the design and development of an energy harvesting system enabling a batteryless, wireless temperature-sensing data logger, intended for monitoring cargo conditions during maritime transport. The system harvests energy via inductive coupling, where a low-profile receiver coil captures power from an alternating magnetic field generated by a ceiling-mounted transmitter coil.

This study specifically addresses key design considerations such as coil design, resonance-matching, Schottky-diode-based rectifification, robust voltage regulation by means of a buck-boost converter and a dual-capacitor energy storage scheme for reliable energy storage and voltage stability.

The design overcomes core challenges in long-range wireless power transfer (WPT) including efficient energy extraction under low-power conditions, stable voltage regulation, and reliable start-up and operation within the constraints of a shipping container.

The prototype achieves stable 2.1V output from harvested energy alone, operating effectively at distances up to 1.4 m, while simulations confirm feasibile operation at the required 2.4 m range intended for its real-life application. The proposed solution achieves a self-sustaining, maintenance-free approach to temperature monitoring, enhancing cargo safety and contributing to the reduction of electronic and food waste. This system offers a scalable, adaptable, low-maintenance alternative to disposable battery-powered sensors, Improving sustainable cold-chain conditions monitoring and adhering to EU electromagnetic exposure limits.

Glossary

An overview of key terms and abbreviations, organized in alphabetical order:

- · General Terms:
 - PoR: Programme of Requirements
- · Technical Terms:
 - AC & DC: Alternating- & Direct Current
 - **Buck-boost converter:** A component used for voltage stabilization.
 - CMOS: Complementary Metal-Oxide Semiconductor
 - Coupling Coefficient (k): A measure relating the mutual inductance between transmitter and receiver
 coils to their self-inductances.
 - **E-waste:** Electronic waste, such as battery-powered sensors, significant source of global pollution.
 - **EMF**: Electro Motive Force
 - Energy Harvesting: The process of capturing and converting ambient energy (e.g., magnetic fields) into usable electrical energy to power devices.
 - ESR: Equivalent Series Resistance
 - FBR: Full-Bridge Rectifier
 - FBR D2: Full-Bridge Rectifier followed by 2 diode charge pumps.
 - GR2: Greinacher Doubler
 - HWR: Half-Wave Rectifier
 - IPT: Inductive power transfer, a method of wirelessly transferring energy through magnetic fields.
 - LTspice: Simulation software used for performance assessments.
 - Magnetic Flux Density: A measure of the strength of a magnetic field, measured in Tesla and often denoted with symbol B.
 - MCU: Micro Controller Unit
 - MOSFET: Metal-Oxide Semiconductor Field-Effect Transistor
 - Mutual Inductance (M): A property that relates the magnetic flux linkage of a receiver coil to the current in a transmitter coil.
 - NFC: A Near-Field Communication, used for wireless data readout and as an energy source for jumpstarting the system.
 - PCE: Power Conversion Efficiency
 - PV: Photovoltaic
 - Rectifier: A circuit component responsible for AC-to-DC conversion of harvested energy.
 - Resonance Matching: The process of adjusting compensation capacitors to ensure that both the transmitter and receiver coils resonate at the same frequency as the source, optimizing performance and power transfer.
 - RF: Radio Frequency
 - Rx: Receiver
 - Schottky diode: Special type of diode, their low forward voltage drop and high efficiency makes them ideal for ultra low-power applications.
 - Self-inductance (L): A property of a coil that describes its ability to induce a voltage in itself due to a changing current.
 - **Supercapacitor:** A passive component commonly used for energy buffering and storage.
 - Tx: Transmitter
 - WPT: Wireless Power Transfer
 - Zener diode: A protective component added in parallel with the output to act as an over-voltage protection mechanism, clamping the voltage to a safe level.

Contents

| 1 | Intro | oduction | 1 |
|---|-------|--|---|
| | 1.1 | Situation Assessment | 1 |
| | 1.2 | Scoping Analysis | |
| | 1.3 | Bounding Analysis | 2 |
| | 1.4 | System Overview | |
| | 1.5 | Report Outline | |
| • | | · | 4 |
| 4 | | gramme of Requirements Requirements | • |
| | ۷. ۱ | 2.1.1 Mandatory Requirements | |
| | | 2.1.2 Trade-off Requirements | |
| | | 2.1.3 Summary of the Requirements | |
| | 2.2 | Key Performance assessment metrics | |
| | 2.2 | 2.2.1 Energy Harvesting Coil | |
| | | 2.2.2 Rectifier | |
| | | | |
| | | 2.2.3 DC-DC converter | |
| | | 2.2.4 (Super)Capacitors | 2 |
| 3 | | | 7 |
| | 3.1 | Energy Harvesting | 7 |
| | | 3.1.1 Types of Energy Harvesting | 7 |
| | | 3.1.2 Energy Harvester - Basic System model | 3 |
| | | 3.1.3 Energy Harvester - Detailed System Model | |
| | 3.2 | Rectifying circuit | 3 |
| | | 3.2.1 Active vs. Passive Rectification | 3 |
| | | 3.2.2 PCE and Peak Power Simulations | 3 |
| | | 3.2.3 The Selected Rectifier Topology | C |
| | | 3.2.4 Output Voltage Stabilization (DC-DC conversion) | J |
| | | 3.2.5 Over-voltage Protection | 1 |
| | | 3.2.6 Equivalent Input Impedance | 1 |
| | | 3.2.7 The Proposed Rectifier - Circuit | |
| | 3.3 | Energy Storage | |
| | | 3.3.1 Energy Storage Options | |
| | | 3.3.2 Modelling (Super)capacitor non-idealities | |
| | | 3.3.3 Sizing the capacitors: Dual Capacitor Energy Storage | |
| | | 3.3.4 The Start-Up and NFC Energy Harvesting Capabilities | |
| | _ | | |
| 4 | Res | | |
| | 4.1 | Prototype Design and Implementation | |
| | | 4.1.1 Prototype - Energy Harvesting System | |
| | | 4.1.2 Prototype - Rectification, Output Stabilization and Energy Storage | |
| | | 4.1.3 Prototype - Final Design and Components | |
| | 4.2 | Designing for a Market Product | |
| | | 4.2.1 Market Product - Necessary Alterations | |
| | | 4.2.2 Market Product - Validation of the Coil Approximation Method | |
| | | 4.2.3 Market Product - Misalignment Prevention | |
| | | 4.2.4 Modifications to the Rest of the System | 3 |
| 5 | Disc | eussion 34 | 4 |
| _ | 5.1 | Key (Experimental) Findings | |
| | - | Limitations and Trade-offs | |

| | 5.3 Lessons Learned | 35 |
|---|--|----------------------|
| 6 | Conclusion | 36 |
| Α | Appendix A - Extended Theory A.1 Energy Harvester - Further Compensation Methods | 39 39 41 |
| В | Appendix B - Simulations and Measurements B.1 Simulations and Measurements | 44 44 45 |
| С | Appendix C - Code C.1 Impedance Analyser Readings C.2 OC Voltage vs Distance Plots C.2.1 LT-spice Simulation Results C.2.2 Measurement Results C.3 Rectification, Protection and Output Stabilization Measurements C.4 Complete system SPICE Netlist | 48 48 49 49 |
| D | Appendix D - List of Used Components D.1 List of Components | 52 |

1

Introduction

1.1. Situation Assessment

Globalization has dramatically improved global access to goods, but has also led to lengthened supply chains and delivery times. This has led to a rise in cold-chain logistics for the transportation of perishable goods such as fresh foods and pharmaceuticals. In these temperature-controlled supply chains precise condition monitoring is critical, as even brief deviations can cause spoilage, shorten shelf life, and drive food waste[7].

The widespread adoption of battery-powered sensors in logistics monitoring carries a significant hidden cost: discarded devices now form a substantial portion of global e-waste. In 2022 alone, global electronic waste (defined as any device "with a plug or battery") reached a record 62 million tonnes. Yet less than one-quarter (22.3%) was properly collected and recycled, leaving billions of dollars worth of hazardous materials to pollute ecosystems and endanger human health [35], [1]. Small appliances and devices, including wireless temperature and condition sensors, account for roughly one-third of this volume, yet only 12% of such small-equipment e-waste is recycled [2].

Breaking free from batteries (electrochemical energy storage devices [9]), has proven challenging. However, energy harvesters combined with high-energy-density storage capacitors offer a promising alternative, providing longer lifespans, lower environmental impact, and reduced maintenance requirements [21]. While early solutions harvested magnetic fields, their effective range was severely limited (typically under one meter) rendering them impractical for shipping-container monitoring. Standard inductive power transfer (IPT) efficiency rapidly diminishes with distance, demanding coil separations of just centimetres for effective coupling [30]. Although ferrite cores or strong magnets can enhance coupling, they increase cost, weight, and size, obstructing the path to truly miniaturized, low-cost sensors [39].

Contemporary commercial magnetic harvesters still confront major obstacles. Operating at the sub-1 MHz frequencies typical in industrial settings, they frequently achieve power-transfer efficiencies below 10% beyond a few centimetres. Consequently, these systems typically deliver only tens of micro watts at distances of three to six meters, which is insufficient for the >100 µW often required by a wireless temperature sensor [11]. This limitation forces either repeated manual realignment or reliance on supplementary batteries, undermining the fundamental goal of a maintenance-free, sustainable sensor network.

This thesis introduces a disposable, temperature monitoring platform designed for large-scale logistics, that does not rely on electrochemical energy storage devices, to overcome these limitations. Its core innovation is a long-range magnetic field harvester capable of stable power delivery at distances up to 2.4 meters. Combined with a low profile receiver coil that minimizes misalignment effects, the system targets robust, hands-off operation within shipping containers. Resonance matching ensures peak efficiency despite variable load and positioning. Together, these advances offer a low-cost, environmentally responsible solution that bridges the gap between magnetic harvesting's practical reach and global supply chain demands, paving the way for scalable, reduced-waste logistics monitoring.

1.2. Scoping Analysis

Modern supply chains involve diverse stakeholders facing a shared challenge. Logistics providers need maintenance-free sensors capable of operating reliably at large distances without battery replacements. Environmental regulators demand significant reductions in the mountains of discarded batteries frequently ending up in landfills [35]. Simultaneously, manufacturers require a solution scalable for mass production, using materials compatible with safe recycling.

Addressing these converging needs, this thesis proposes an integrated solution centred on a long-range magnetic harvester. Tuned to a specific frequency and built around a large transmit coil, this subsystem must reliably output at least 2.1 μ W (required to power the MCU [3]) in standby mode. Crucially, it must also deliver bursts of up to 840 μ W to power data sampling and wireless transmission [3] during active sensor operation. To achieve stringent cost and size targets, the receiver coil is designed as a ring attached onto a flat sheet. This geometry minimizes the overall footprint while inherently preventing total coil misalignment. Surplus energy is buffered by a combined capacitor and supercapacitor storage system, ensuring brief field interruptions do not disrupt monitoring.

Achieving these metrics would fulfil every stakeholder requirement: a truly hands-off sensor network for logistics; a dramatic reduction in disposable battery waste; and a mass-manufacturable module with a highly affordable production cost. Success is defined by obtaining a consistent 2.1 μ W output at a separation of 2.4 meters (typical height of a standard container) while keeping the receiver coil radius under 12 cm. Detailed simulations will optimise coil parameters and circuit components, followed by experimental validation. In doing so, this work establishes a practical foundation for sustainable, cost-effective condition monitoring across global supply chains.

1.3. Bounding Analysis

Compliance with the EU Directive 2013/35/EU is mandatory. This regulation limits magnetic flux density to 100 μ T for frequencies under 100 kHz to protect worker health [27]. Compliance with the EU Council Recommendation 1999/519/EC, limiting flux density to 6.25 μ T [34] in public contexts is desirable but not strictly necessary given the device's intended use in the logistics sector.

The prototype's transmitter coil parameters are fixed, establishing a baseline against which the receiver and matching network must be tuned. Economically, the entire harvesting subsystem (excluding the transmit coil, sensor and MCU) must cost under €70 in production volumes. Given the wide price range of high-performance components, meticulous selection is essential to meet this budget target.

The receiver employs a spiral ring-shaped copper coil mounted on a flat backing as the primary energy capture mechanism. The number of windings and core dimensions will be optimised to maximize mutual inductance and quality factor while accommodating potential misalignment. Captured energy is buffered by a combined capacitor and supercapacitor. These components must be selected for sufficient capacitance and voltage rating to bridge short transmitter outages, all while adhering to self-discharge and size constraints.

Following energy capture, a rectification circuit converts the AC- to DC voltage. This is then fed into a DC-DC converter to ensure stable, usable DC voltage charges the supercapacitor buffer. Component selection for the rectifier and converter will leverage established design formulas alongside manufacturer data sheets and user guides. The goal is to maximize power efficiency and minimize insertion loss across anticipated load variations. Together, these defined constraints and optimisation variables establish a clear, technically rigorous development path for a compliant, cost-effective, long-range energy-harvesting subsystem.

1.4. System Overview

Figure 1.1 presents a block diagram of the complete system.

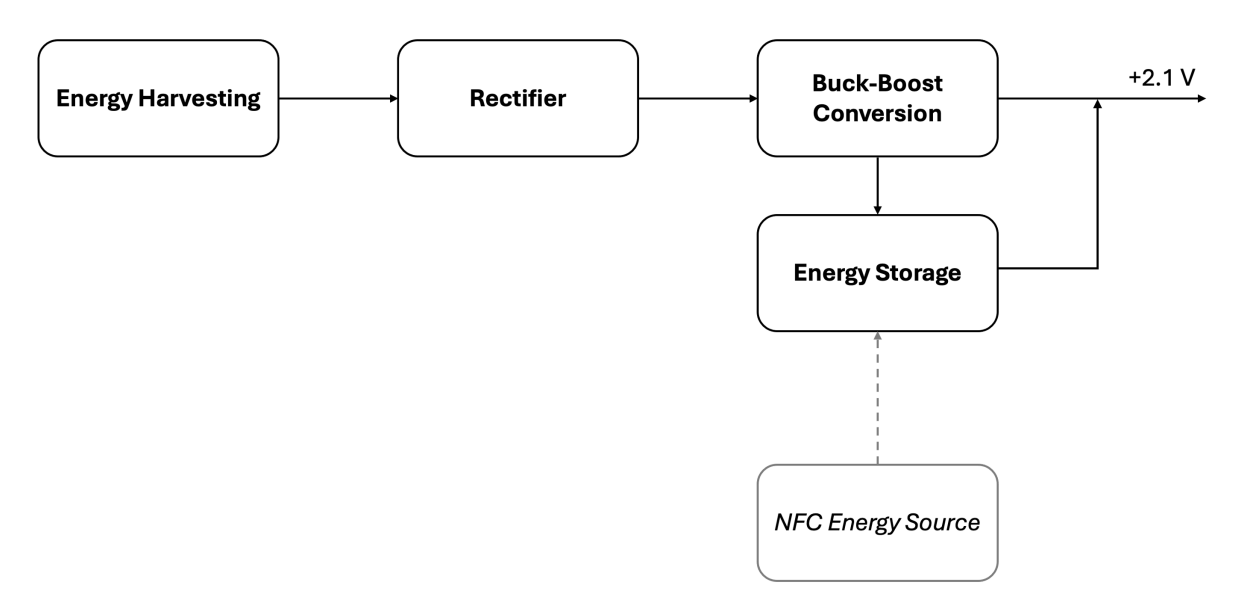


Figure 1.1: This overview details the connections between the various system blocks. Energy harvesting serves as the primary power source, while a rectifier converts AC to DC voltage. A buck-boost converter ensures a stable 2.1 V DC output. Excess energy from the buck-boost converter or the NFC energy source is stored for future use. Note that the NFC energy source is only active during data transfer readings, providing a temporary jump-start or energy boost during those periods.

1.5. Report Outline

This thesis adheres to the following structure:

· Chapter 1: Introduction

Provides an overview of the project background, motivation, and scope; defines the challenges of batteryless sensing in shipping containers and outlines key system constraints and objectives.

· Chapter 2: Programme of Requirements

Outlines all mandatory and trade-off requirements, covering electrical performance, environmental constraints, and usage model. Additionally, it defines key performance metrics for evaluating system components.

· Chapter 3: Theory and Analysis

Establishes the theoretical foundations of inductive energy harvesting, including coil design, resonance matching, and rectification, while also analysing energy storage strategies through mathematical modeling.

· Chapter 4: Results

Details the implementation and measurement of the prototype, whilst also exploring its potential for development into a market product, covering coil construction, rectifier design, and system integration, while evaluating its performance against the specified requirements.

· Chapter 5: Discussion

Analyses experimental findings, explores limitations and trade-offs, reflects on lessons learned, and proposes enhancements for a future design.

· Chapter 6: Conclusion

Summarizes key achievements, validates the completion of project objectives, and proposes future research directions.

Appendices

Provide extended derivations, detailed simulation and measurement data, code listings and a full component list to support the main text.

Programme of Requirements

2.1. Requirements

In order to make informed decisions regarding the design of the device, a clear overview of requirements is listed in this section. The requirements are divided into two main categories: mandatory requirements and trade-off requirements. The mandatory requirements are non-negotiable and must be fulfilled to ensure the fundamental functionality of the system. In contrast, the trade-off requirements represent desirable features that enhance the final product but are not strictly necessary for basic operation. Because the demonstrator is a scale-model of the final product, some requirements that are mandatory for the final product are listed as a trade-off requirement for the demonstrator, an overview of requirements and their type for both demonstrator and the final product are summarized in table 2.1.3.

2.1.1. Mandatory Requirements

The device must meet the following mandatory requirements (grouped by category).

1. Electrical Performance

- The system must deliver a constant and stable 2.1 V DC output at an average power > 2.1 μW to supply the sensor and microcontroller [3].
- In line with the goal of minimizing e-waste, the device should not incorporate batteries; thus reducing the use of environmentally harmful components.
- Must be self-starting without the use of pre-charged capacitors.
- The device must be entirely powered by electromagnetic energy harvested from the inductively coupled beacon coil(s), with the exception of NFC harvested power, received only upon initial device installation and data retrieval.

2. Environmental and Practical Constraints

- System must comply with EU Directive 2013/35/EU, limiting magnetic flux density to under 100μT to protect worker health.
- The device is intended for use within shipping containers and must be functional throughout the volume of a 20 ft container (6.0 × 2.4 × 2.4 m) the position of transmit and receive coils relative to each other are bound by these dimensions. In other words, the device should work at coil distances up to 2.4 meter.
- Prototype budget limited to €70, using self-built or commercially available parts.
- No components should be installed or mounted outside the container; all parts must remain within its confines. For example, mounting the Tx coil to the ceiling is permitted.
- The device must be functional in a temperature range from -30 °C to +50 °C.

3. Usage

• The device should follow a 'set-and-forget' usage model and require no maintenance for the duration of a 4 week journey.

2.1.2. Trade-off Requirements

The following soft requirements are desireable, but not of absolute necessity.

- To preserve cargo capacity and minimize impact, the device should ideally remain relatively low profile and ideally weigh less than 1kg.
- In order to account for time spent in between shipping containers and store shelves the device should remain operational for 5 hours in the absence of a functioning beacon.
- To improve customizability and minimize electronic waste, the device's sub-components (energy harvester, rectifier, and energy storage) should follow a modular design. This approach not only simplifies troubleshooting and iteration during prototyping but also enables the device to be adapted for a broader range of applications.

2.1.3. Summary of the Requirements

| Requirement | Prototype/Demonstrator | Final Product |
|--|------------------------|---------------|
| Output stable ±2.1V DC at >2.1µW | MR | MR |
| Self-starting with no pre-charged capacitors | ToR | MR |
| Powered entirely by harvested energy | MR | MR |
| Compliance with 100µT legal limit | MR | MR |
| Functional at ≥2.4 m coil distance | ToR | MR |
| No external mounting on container | MR | MR |
| Operating temperature –30°C to +50°C | MR | MR |
| Set-and-forget, 4-week operation | MR | MR |
| No battery use | MR | MR |
| Modular, adaptable design | ToR | ToR |
| Prototype built under €70 with available parts | MR | _ |
| Operational for 5 hours in the absence of a beacon | ToR | ToR |
| Maximum weight of 1kg | ToR | ToR |

2.2. Key Performance assessment metrics

In order to assess the viability of specific design choices, key performance indicators for the various subcomponents of the energy-harvesting circuit will be postulated in this section. These metrics will form the basis of design choice justifications.

2.2.1. Energy Harvesting Coil

The pick-up coil is the source of all energy in the system, as such it's performance will be judged by quantities relating to harvested power/ energy. Taking Ohm's law as a foundation the primary performance quality metrics are:

- · Received Open-circuit voltage over distance.
- Receive Coil internal impedance (consisting of resistance and reactance).

2.2.2. Rectifier

After the pick-up coil the harvested electrical energy is rectified, converting an alternating current (AC) into a direct current (DC), as will be explained in later sections this rectification is not a lossless process. The performance assessment metrics for the rectifier concern the handling of harvested power. The key performance metrics are as follows:

- Rectifier peak output power and voltage over distance and the trade-off involved in optimising one over the other.
- Power conversion efficiency (PCE) over distance.

2.2.3. DC-DC converter

Post rectification DC-DC conversion will likely be necessary to protect sensitive downstream components such as the capacitive energy banks and microcontroller from the wide range of possible input voltages. The key performance indicators for this part are:

- Absolute maximum and minimum received input voltage/power (wider ranges preferred).
- · Quiescent current leakage.
- · Minimum operating input power.
- · DC output voltage over distance

2.2.4. (Super)Capacitors

To supply the MCU's hourly power burst and to store surplus harvested energy, a capacitive energy storage bank is positioned at the output of the DC-DC converter. The following performance indicators are essential for evaluating its effectiveness.

- Leakage current/ equivalent parallel self-discharge resistance.
- Capacitance, detrimental for active cycle energy and sets limit on device lifetime in the absence of harvestable energy.
- · System start-up time.
- Equivalent Series Resistance (ESR), to be used as a metric for assessing robust handling of transient current spikes.



Theory and Analysis

3.1. Energy Harvesting

This section explores the primary driver of the system: energy harvesting, beginning with an analysis of its different types.

3.1.1. Types of Energy Harvesting

Powering sensors in sealed shipping containers requires evaluating ambient energy sources. Four primary methods are analysed below for operating principles, container implementation constraints, and projected energy yield versus complexity/cost.

Solar Energy

Photovoltaic (PV) cells convert sunlight to electricity, achieving 15–22% efficiency (yielding tens-hundreds mW/cm² at 1000 W/m²) [19]. However, standard steel containers block all sunlight internally. External PV mounting requires structural modifications/penetrations, which are prohibited by the PoR, making solar unviable for sealed containers without external access.

RF Energy

Radio frequency (RF) energy harvesters convert ambient electromagnetic signals (Wi-Fi, cellular) to DC power via antenna and rectifier. Typical urban power densities are tens-hundreds μ W/m² [5]. While RF ICs are efficient, this low output necessitates complex, costly external high-gain antennas and feeds through the metal wall to meet the project's microwatt requirements, rendering it impractical, as it would go against multiple requirements concerning cost and power yield.

Thermal and Vibration Energy

Thermoelectric generators (TEGs) use the Seebeck effect to convert temperature gradients (ΔT) into electricity, producing 20–50 μ W/cm² per 10 K ΔT [25]. Sealed containers exhibit infrequent, modest internal temperature fluctuations. Crucially, exploiting ambient temperature differences requires external mounting/heat exchange, violating the intrusion-free requirement and making TEGs unsuitable.

Similarly, vibration energy harvesting relies on mechanical oscillations but suffers from extremely low power yields, typically in the μ W range. The challenge of efficiently capturing and converting sporadic, low-amplitude vibrations further limits its practicality in most applications.

Magnetic-Field Energy

Inductive coupling uses a time-varying magnetic field between transmitter and receiver coils, inducing AC current at the receive side. At close distances (cm), efficiencies >70% and power levels up to hundreds of mW are achievable [14]. Both coils can reside inside the container, separated only by a thin non-metallic barrier (e.g., window), with minimal flux loss. Near-field operation (10–500 kHz) penetrates composites efficiently. It requires no line-of-sight, external components, or temperature difference, delivering microwatts-milliwatts continuously at moderate cost via factory integration or service ports. Magnetic-field coupling is thus the ideal method, providing reliable power without compromising container integrity.

3.1.2. Energy Harvester - Basic System model

The temperature-sensing data logger operates through energy harvesting, utilizing a magnetic field generated by a transmitter coil. The transmitter consists of a large coil conducting an alternating current, thereby inducing a magnetic field. Magnetically coupled to the transmitter is a pick up coil, specifically designed to capture and convert the energy from the generated magnetic field.

The system can be modelled as a coupled transmitter-receiver coil configuration, in which the beacon functions as the transmitter, while the pickup coil serves as the receiver. Figure 3.1 presents a simplified representation of the circuit.

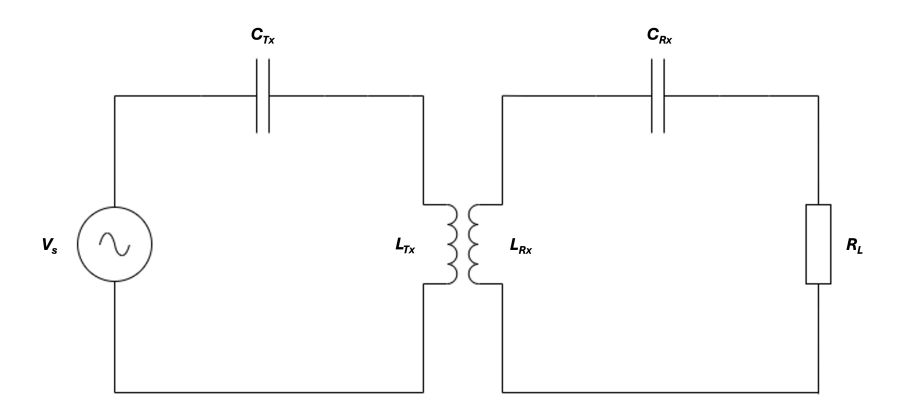


Figure 3.1: Simplified circuit schematic, where V_s , L_{Tx} , L_{Rx} , C_{Tx} , C_{Rx} , and R_L represent the source voltage, transmitter (Tx) and receiver (Rx) inductance and resonance compensation capacitance, and the load, respectively.

To accurately model this system with the objective of designing an efficient configuration, the process begins at the transmitter side.

Theory - Magnetic Field and Mutual Inductance

Figure 3.1 presents a highly simplified model of the system. For a more precise representation, a detailed analysis of the individual component interactions is necessary.

Magnetic Field

A singular winding of the circular transmitter (Tx) coil used in protoyping can be modelled as a loop, with radius R_{Tx} , as seen in Figure 3.2.

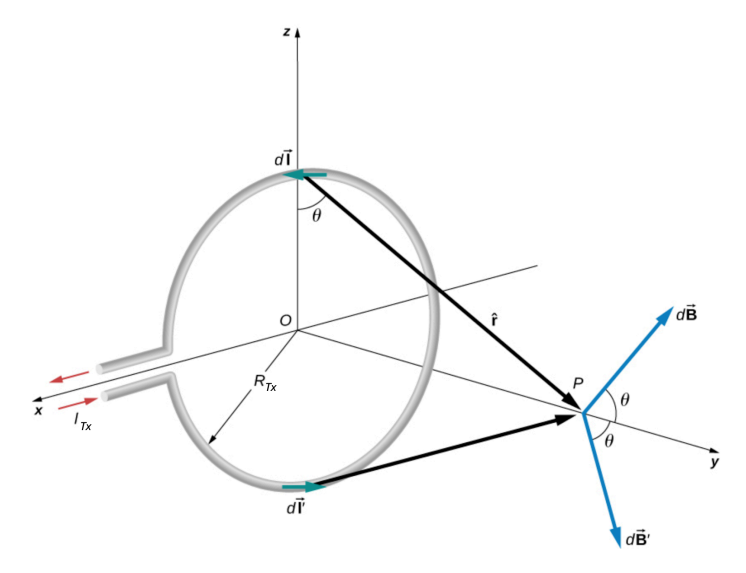


Figure 3.2: Circular loop with radius R_{Tx} , carrying a current I_{Tx} . Based on the figure presented in [8].

The Biot-Savart law describes the magnetic field generated by a current and is defined as [23]:

$$d\mathbf{B} = \frac{\mu_0}{4\pi} \frac{I\mathbf{dl} \times \mathbf{r}}{r^2} \tag{3.1}$$

In the case of a point P on the y-axis, aligned with the centre of a tightly wound, air core, Tx-coil with N_{Tx} windings, this simplifies to:

$$B_{Tx}(y) = \frac{\mu_0 I_{Tx} N_{Tx} R_{Tx}^2}{2(R_{Tx}^2 + y^2)^{3/2}} \quad [T]$$
 (3.2)

Where B_{Tx} is the magnetic flux density in Tesla, y the orthogonal distance from the center of the loop, I_{Tx} is the current through the loop, R_{Tx} the radius of the loop and μ_0 the permeability of free space ($\mu_0 = 4\pi \cdot 10^{-7}$ [H/m]).

Magnetic Flux and Induced Voltage

The receiver (Rx) coil, having N_{Rx} windings and area $A_{Rx} = \pi R_{Rx}^2$ intercepts a flux:

$$\Phi_{Rx} = N_{Tx}B_{Tx}(y)A_{Rx}\cos\theta \quad [Wb]$$
(3.3)

where θ is the angle between the magnetic field and the normal of the Rx coil's plane (with $\theta = 0$ for perfect alignment). According to Faraday's law[23], the open-circuit (AC) induced voltage in the Rx coil is

$$V_{oc} = -j\omega \,\Phi_{Rx} = -j\omega \,B_{Tx}(y) \,A_{Rx} N_{Rx} \quad [V]$$

$$\tag{3.4}$$

Taking the peak magnitude results in

$$|V_{QC}| = \omega B_{Tx}(y) A_{Rx} N_{Rx} \quad [V]$$
 (3.5)

Mutual Inductance and Coupling Coefficient

The mutual inductance[6] M between the Tx- and Rx-coils relates the flux linkage of the Rx-coil to the Tx current:

$$M = \frac{N_{Rx} \Phi_{Rx}}{I_{Tx}} \quad [H] \tag{3.6}$$

Substituting the expression for $B_{Tx}(y)$ derived in 3.2, one obtains

$$M = \frac{\mu_0 R_{Tx}^2 N_{Rx} N_{Tx} A_{Rx}}{2 (R_{Tx}^2 + y^2)^{3/2}}$$
 [H] (3.7)

The coupling coefficient k is defined as

$$k = \frac{M}{\sqrt{L_{Tx} L_{Rx}}} \tag{3.8}$$

where L_{Tx} and L_{Rx} are the self-inductances of the Tx and Rx coils, respectively.

Self inductance can then be estimated by [24]:

$$L = N^2 \cdot \mu \cdot d(\ln(\frac{8d}{t} - 2)) [H]$$
(3.9)

Where $\mu = \mu_r \mu_0$ is core permeability, d is loop diameter, N is number of windings and t is wire thickness.

3.1.3. Energy Harvester - Detailed System Model

When taking real world losses and the mutual inductance between Tx and Rx coils into account, the circuit diagram displayed in Figure 3.1 can be expanded into the diagram seen in Figure 3.3.

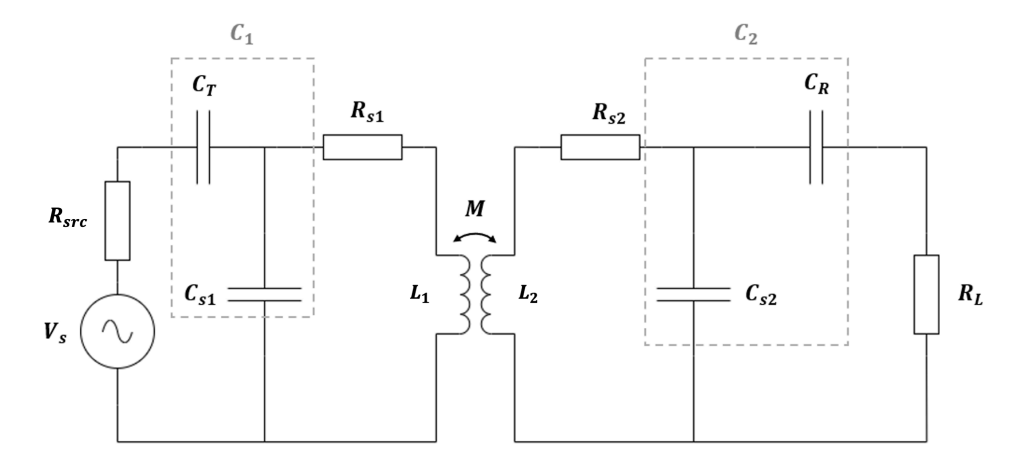


Figure 3.3: Tx-Rx coupled coil equivalent circuit, largely based on the circuits presented in [10] and [38].

In Figure 3.3, $L_1 = L_{Tx}$ and $L_2 = L_{Rx}$ represent the self inductances of the Tx and Rx coils, respectively. Similarly, R_{s1} and R_{s2} denote the parasitic coil resistances, while C_{s1} and C_{s2} account for the parasitic capacitances. To ensure source resonance, C_T and C_R serve as the resonance compensation capacitors for the Tx and Rx coils. Additionally, R_{src} and R_L correspond to the source and load resistances, respectively. The load resistance represents the rest of the system modelled as a single resistance.

Theory - Circuit Analysis

The primary (Z_1) , secondary (Z_2) and mutual (Z_M) impedances in Figure 3.3 are defined as:

$$Z_{1} = R_{\text{src}} + R_{s1} + \frac{1}{j\omega C_{1}} + j\omega L_{1},$$

$$Z_{2} = R_{s2} + R_{L} + \frac{1}{j\omega C_{2}} + j\omega L_{2},$$

$$Z_{M} = j\omega M$$
(3.10)

Where,

• C_1 is formed by C_T and C_{s1} in series:

$$\frac{1}{C_1} = \frac{1}{C_T} + \frac{1}{C_{S1}} \Rightarrow C_1 = \left(\frac{1}{C_T} + \frac{1}{C_{S1}}\right)^{-1}$$
(3.11)

• C_2 is formed by C_{S2} and C_R in series:

$$\frac{1}{C_2} = \frac{1}{C_{s2}} + \frac{1}{C_R} \Rightarrow C_2 = \left(\frac{1}{C_{s2}} + \frac{1}{C_R}\right)^{-1}$$
 (3.12)

To analyse the circuit, the mesh currents are defined as:

- I1: current in the primary (source side) loop
- I_2 : current in the secondary (load side) loop

Applying Kirchoff's voltage law, the mesh equations can be found for the primary and secondary mesh:

$$\begin{cases}
-V_S + Z_1 I_1 - Z_M I_2 = 0 \\
-Z_M I_1 + Z_2 I_2 = 0
\end{cases}$$
(3.13)

Solving for the currents gives:

$$\begin{cases} I_1 &= \frac{V_s Z_2}{Z_1 Z_2 - Z_M^2}, \\ I_2 &= \frac{V_s Z_M}{Z_1 Z_2 - Z_M^2} \end{cases}$$
(3.14)

With this, the voltage across the load can be found as:

$$V_L = I_2 R_L = \frac{V_s Z_M}{Z_1 Z_2 - Z_M^2} \cdot R_L \quad [V]$$
 (3.15)

As the goal is to deliver the maximum amount of power to the load, the following conditions should be met:

1. Resonance condition:

$$\omega = \frac{1}{\sqrt{L_1 C_1}} = \frac{1}{\sqrt{L_2 C_2}} \Rightarrow \frac{1}{j\omega C_1} + j\omega L_1 = 0, \quad \frac{1}{j\omega C_2} + j\omega L_2 = 0$$
 (3.16)

So only the real part of the impedances remains:

$$Z_1 = R_{\rm src} + R_{\rm s1}, \quad Z_2 = R_{\rm s2} + R_L$$
 (3.17)

This ensures no imaginary component to the impedance and thus purely real transfered power.

2. Matched Load:

$$R_L = R_{s2} \Rightarrow Z_2 = 2R_L \tag{3.18}$$

Now, to work towards finding the voltage over the load, start from the primary mesh:

$$V_S = I_S Z_1 - I_2 Z_M \Rightarrow I_2 = \frac{(I_S Z_1 - I_2 Z_M) Z_M}{Z_1 Z_2 - Z_M^2}$$
(3.19)

Solving for I_2 in terms of I_s :

$$I_2\left(1 + \frac{Z_M^2}{Z_1Z_2 - Z_M^2}\right) = \frac{I_sZ_1Z_M}{Z_1Z_2 - Z_M^2} \Rightarrow I_2 = \frac{I_sZ_1Z_M}{Z_1Z_2} = \frac{I_sZ_M}{Z_2}$$
(3.20)

Then:

$$V_L = I_2 R_L = \frac{I_s Z_M R_L}{Z_2} \Rightarrow V_L = \frac{j\omega M}{2} \cdot I_s [V]$$
(3.21)

Here, the complex j indicates that the load voltage leads or lags the source current by 90° . The magnitude of the voltage over the load is:

$$|V_L| = \frac{\omega M I_s}{2} \quad [V] \tag{3.22}$$

Finally, having obtained an expression for the matched load voltage, the power and energy delivered to the load can also be found[6]:

$$P_L = \frac{V_L^2}{R_L} \quad [W] , \quad \boxed{E_L = P_L \cdot t \quad [J]}$$
(3.23)

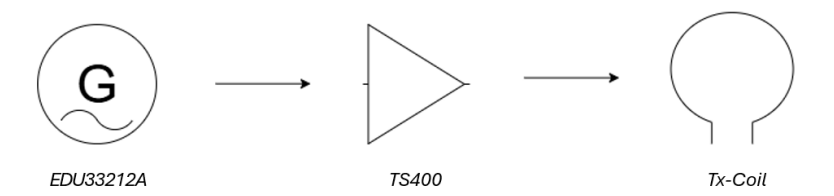


Figure 3.4: Simple overview of the Tx-setup.

Transmitter Coil

Since a full design for the beacon/Tx-coil falls outside the scope of this project, a straightforward approach has been adopted for its selection.

As mentioned earlier, the transmitter coil is driven by a function generator, the *EDU33212A* [12], serving as the signal source. This source is then connected to an *Accel Instruments TS400* voltage/current amplifier [4], which amplifies the signal before feeding it into the Tx coil. Figure 3.4 presents a simplified diagram of this setup.

The Tx-coils used in this study are the same type utilized in the *EE3C11* Electronics course. Their characteristics are presented in Table 3.1.

| Parameter | Stated Value | Measured Value (UTP wire) | Measured Value (Audio wire) | Calculated Value (2 Audio wire coils in parallel) |
|---------------------------|--------------|---------------------------|-----------------------------|---|
| Self Inductance | 314 µH | 308 μH | 275 μΗ, 38.4 μΗ | 42 μH |
| Parasitic Resistance (DC) | 8.099 Ω | 8.35 Ω | 1.3 Ω, 1.5 Ω | 0.42 Ω |
| Parasitic Capacitance* | 109 pF | Not Measured | 1.49 pF, 0.21 pF | 1.67 pF |
| Windings (N) | 8 | 8 | 8, 8 | 4 |
| Radius | 67.5 cm | 67.5 cm | 67.5 cm, 67.5 cm | 67.5 cm |

Table 3.1: Characteristics of beacon coils constructed from different materials (UTP and two audio wire coils), including values provided on the EE3C11 page [32], measured values, and calculated values. The Tx-coil (both materials) can tolerate between 0.5 to 3 amperes of current. Due to range limitations, the LRC measurement tool used to measure inductance, resistance, and capacitance was unable to read the capacitance of the coils; their parasitic capacitance was later calculated using resonance frequency found via an impedance analyser.

The findings from this theoretical analysis will inform the design and development of the prototype. The insights obtained from both the prototype and this study will serve as a foundation for further refinement and optimization of the beacon, facilitating the transition toward a fully developed market-ready product.

Frequency Analysis

A spectrum analyser was used to perform a frequency analysis on the audio wire coils. The result of this can be seen in Figure 3.5.

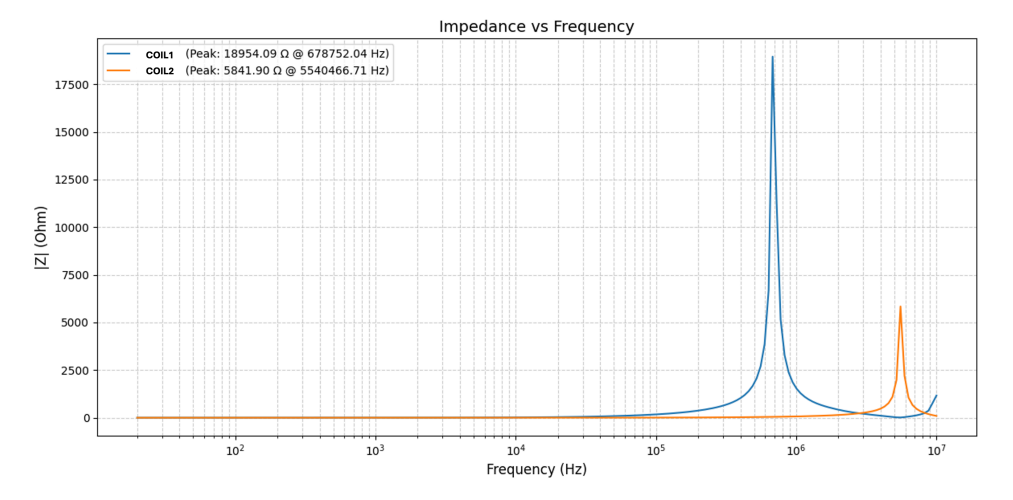


Figure 3.5: The impedance as a function of frequency is presented in the diagram. It is observed that at the self-resonance frequency, the impedance of the coils reaches its maximum. In the diagram, COIL1 and COIL2 denote coil 1 (275 μ H) and coil 2 (38.4 μ H), respectively. The raw data and the script used for plotting can be found in Appendix C.1.

From the analysis, the self-resonance frequencies of the coils were determined as follows:

• Coil 1 (275 μH): 678.75 kHz

• Coil 2 (38.4 μH): 5.54 MHz

These frequencies enable the calculation of the parasitic capacitances of the coils using the resonance condition described in Eq. 3.16. Additionally, it is important to note that near these frequencies, the coil impedance significantly increases, resulting in substantial power loss. Therefore, to ensure efficient operation, the driving frequency should be chosen well below or well above the resonance frequency, the latter being unfeasible as standard function generators generally don't operate at such high frequencies.

When it comes to driving the circuit on the transmitter side, a trade-off has to be made. Without a compensation capacitor, the impedance of the Tx-coil is defined as $Z_L = j\omega L_{Tx} = \frac{V_s}{I_s}$, this can be rewritten to the form:

$$|f| = \frac{V_S}{2\pi L_{Tx} I_S} \tag{3.24}$$

As the maximum output voltage of the function generator is 10 V, the source frequency is directly dependent on the Tx-coil self inductance and the source current.

Since the operating frequency is well below the coil's self-resonance frequencies, the effects of the parasitic capacitance become insignificant. As a result, the coils can be modeled as a series combination of their inductance and a small resistive loss. When an AC source is applied under these conditions, the voltage drop across the resistor is minor compared to the voltage associated with the inductive reactance. Owing to the 90° phase difference between these voltage components, their vector (phasor) sum is nearly equal to the applied source voltage. In essence, when operating far below the self-resonance frequency, the voltage appearing across the coil is effectively the same as the source voltage V_{\circ} .

Based on experimental results and its low inductance value, as seen in Table 3.1, coil 2 (38.4 μ H) was identified as the optimal choice. Further evaluation of the prototype using coil 2 revealed that its ideal operating frequency is approximately 36.48 kHz. At this frequency, the receiver achieves optimal open-circuit voltage, as discussed in greater detail in Chapter 4.1.

Receiver Coil

In accordance with the theoretical analysis presented in Section 3.1.3, optimizing the receiver (Rx) coil is essential for achieving maximum power transfer to the load. The design parameters of the Rx coil (specifically, the number of turns N_{Rx} , the self-inductance L_{Rx} , and the coil geometry) directly influence the induced voltage, as expressed in Equation 3.5. In practice, increasing the number of turns enhances the induced electromotive force (EMF); however, it also increases parasitic resistance and stray capacitance, which may negatively impact efficiency.

One effective solution is to use enamelled copper wire, ensuring the right wiring gauge, where the wire has a diameter no greater than 2δ , where δ is the skin depth defined by

$$\delta = \frac{1}{\sqrt{\pi f \mu \sigma}} [m] \tag{3.25}$$

where f, μ , and σ denote the frequency, permeability of the conductor, and conductivity, respectively.

Using an appropriate wire gauge for coil winding significantly reduces parasitic resistance and capacitance. Given this, Equation 3.9 can be used to estimate the inductance of a self-wound coil. To achieve a compact design while ensuring sufficient coil area, an outer radius between 10 and 12 cm is selected, in accordance with the PoR. Additionally, a flat coil is preferred due to its favourable geometric properties, offering a large surface area while remaining unobtrusive. This helps maintain a low-profile design, as required by the PoR. Furthermore, this configuration allows for more precise parameter approximations, making it a practical choice for optimization.

Furthermore, according to Equations 3.7 and 3.22, a trade-off must be made when determining the optimal number of windings. The objective is to achieve sufficiently high mutual inductance while mitigating excessive self-inductance, thereby maximizing the load voltage. This optimization is necessary to enhance the coupling factor. On the receiver (Rx) side, this can be accomplished by adjusting the number of windings (N_{Rx}) and the radius (R_{Rx}) of the Rx coil, while maintaining a subtle design approach. Table 3.2 presents three realistic combinations selected for their favourable performance parameters.

| Inductance [mH] | Windings N | Radius [m] | Average coil height [m] |
|-----------------|------------|------------|-------------------------|
| 96 | 325 | 0.10 | 0.02 |
| 92 | 300 | 0.11 | 0.02 |
| 92 | 275 | 0.12 | 0.02 |

Table 3.2: For the creation of a prototype, inductance values for two N and radii combinations were calculated using Equation 3.9, assuming $\mu_T = 1$ for an air-core coil. The options presented in the table, were the most favourable and, according to simulations, provided satisfying voltage and power yields at desired distances.

Coil Geometry

The coil is designed as a flat ring mounted on a rigid plastic square backing, ensuring structural stability. Due to the low centre of mass, this flat configuration minimizes the risk of misalignment with the beacon, as it naturally settles in the correct orientation when placed. Thanks to its lightweight and balanced design, the coil can simply be dropped or positioned without precise placement, reliably landing with its top facing the ceiling coil for optimal alignment. Figure 3.6 illustrates this setup.

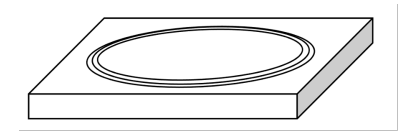


Figure 3.6: A schematic representation of the manufactured coil design, illustrating its physical structure. The remainder of the circuit (including the MCU, sensor, and other components) can be concealed behind the plastic backing, ensuring a clean and unobtrusive appearance.

If placed on an uneven surface, the coil may become slightly misaligned, resulting in an angle offset. However, as demonstrated in Chapter 4.1, unless the offset is extreme, the impact will remain negligible. This

eliminates the need for three-dimensional coils, which would be too large, compromising the low-profile design, and thus conflict with the PoR. Chapter 4.2 explores even more effective alternatives for the market product, such as multiple beacon coils, which further minimize the risk of misalignment.

System Yield

To evaluate the performance of the transmitter (Tx) and receiver (Rx) circuit, simulations were conducted using LTSpice and the equations from Section 3.1.3 to observe the theoretical open-circuit voltage. The simulation assumes minimal losses and proper coil alignment, providing an estimation of system behaviour. Figure 3.7 illustrates how the open-circuit voltage varies as the distance increases up to 2.4 meters.

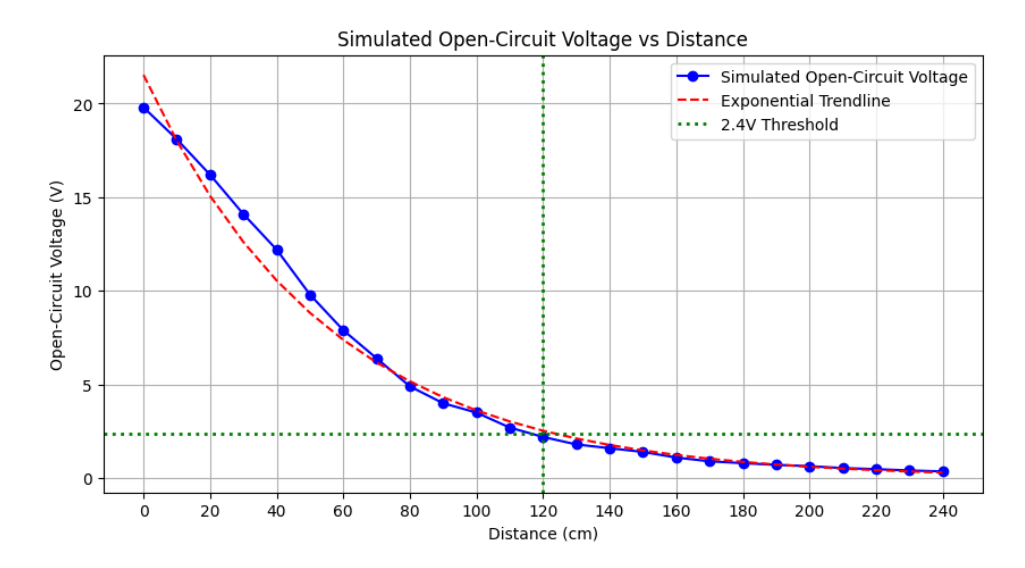


Figure 3.7: Expected load voltage and power, for the 38.4 μ H Tx coil from table 3.1 and the middle Rx coil from table 3.2: $N_{Tx} = 8$, $I_{Tx} = 1$ A, $R_{L} = 5$ M Ω , $N_{Rx} = 300$, $R_{Rx} = 11$ cm and f = 36.48 kHz. No resonance compensation capacitors were added in this simulation.

The results indicate that, for the prototype, the voltage reaching the load is sufficient at distances up to and including 1.2 meters, aligning with the PoR requirements. However, for the market product, the PoR specifies a required transmission distance of 2.4 meters; the approach to achieving this is discussed in greater detail in Chapter 4.2. If the voltage reaching the load is insufficient (\leq 2.4 V) to effectively drive subsequent circuit stages (including rectification and the buck-boost converter) a compensation method will be required to enhance power transfer efficiency. This scenario is further explored in Appendix A.1.

3.2. Rectifying circuit

The induced voltage in the receiver pick-up coil will be an alternating current of the same frequency as the transmitter, since the MCU and sensor need a stable DC voltage of at least 1.7 V to operate and a capacitor cannot accumulate charge from an unbiased AC voltage, a rectifying stage is required. The rectifier will need to convert the incoming AC signal from the output of the pick-up coil to a DC voltage large enough to effectively power a DC-DC converter and MCU. This section presents a comparison and analysis of commonly used rectification techniques as well as a justification for the chosen rectifier.

Assumptions and Boundary Conditions

For this section it is assumed the AC input voltage produced by the magnetically coupled pickup coil can be approximated by a perfectly sinusoidal wave. The incoming AC source should be rectified and the output of the rectifier should be high enough to be effectively stepped up or down by the DC-DC converter to produce a stable DC output voltage for the full range of possible coil distances.

3.2.1. Active vs. Passive Rectification

Generally, AC-DC conversion can be achieved using passive components exclusively; the fundamental element of this conversion is the diode.

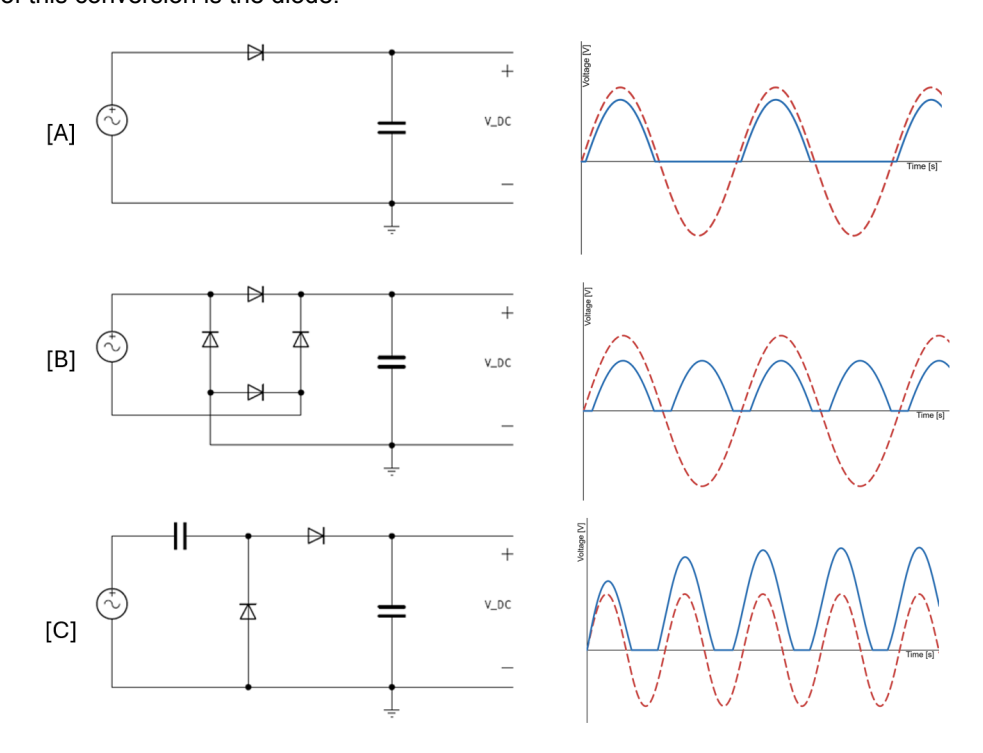


Figure 3.8: Various diode rectifier topologies and their output voltage (blue line) for a sinusoidal input (dotted red line). (A) Half-wave rectifier, (B) Full-bridge rectifier, (C) Greinacher voltage doubler. Although schematics include an output capacitor, the waveforms present rectified signal in the absence of a smoothing capacitor.

Passive Rectifiers and Multipliers

The simplest rectifier is a single diode followed by a capacitor (Figure 3.8A), this so-called half-wave rectifier (HWR) has a limited efficiency, as only the positive half of the AC signal gets through the rectifier and is additionally reduced by the voltage drop of the diode when it is forward biased.

Full-wave rectification can be achieved using a full-bridge rectifier (FBR) composed of four diodes, as shown in figure 3.8B. In this configuration, both halves of the input sinusoidal waveform are rectified, offering improved efficiency compared to half-wave rectification (HWR) [33]. However, since two diodes conduct during each half-cycle, the output voltage is reduced by twice the diode forward voltage, as can be seen in Figure 3.8. Alternatively, if a differential AC signal is available, such as with a center tapped coil, a full wave rectifier can be realised utilising only 2 diodes.

The waveforms in Figure 3.8 illustrate the output voltage in the absence of output smoothing capacitors. These capacitors serve a critical role in reducing output ripple and determining the steady-state response time. The relation between the peak-to-peak output ripple and smoothing capacitance can be approximated by equation 3.26 [22].

$$V_{r(pp)} = \frac{V_m}{f_r \cdot C \cdot R} [V]$$
(3.26)

Where V_m is the peak amplitude of the input AC voltage, f_r is the ripple frequency (2 · f_{in} for a FBR) and R is the load resistance attached to the output of the rectifier.

Passive diode rectifiers are relatively simple and cost-effective circuits when compared to active (CMOS) rectifiers, however they do not come without drawbacks. The main drawbacks are the losses incurred due to forward voltage drop and parasitics associated with the diodes. The output voltage of diode-based rectifiers/multipliers is attenuated by the diode forward voltage drop. Additionally, they require an input voltage greater than the diode forward voltage to allow for any power transfer. This energy barrier and the loss associated with it can be minimized by selecting a diode with a very low forward voltage such as Schottky diodes, these diodes can have forward voltage drops as low as 100 mV. After initial rectification, the voltage can be boosted using a variety of simple diode-capacitor topologies, such as Dickson charge pumps.

Voltage-multiplying rectifiers, like the Greinacher voltage doubler (GR2) seen in 3.8C, can theoretically convert an AC input voltage to a multiplied DC voltage. The mechanism behind this is the charging-up effect of the GR2 input capacitor, introducing a voltage bias at the intermediate node. This DC offset is equal to $V_m - V_{fwd}$ and the DC output voltage of the doubler is equal to $2V_m - 2V_{fwd}$, where V_m is the amplitude of the rectifier input voltage and V_{fwd} is the forward voltage drop of the diode. Multipliers of higher orders are also possible, capable of rectifying an AC input with an amplitude of V_m into a DC voltage equal to:

$$V_{\text{out}} = N(V_m - V_f) \quad [V] \tag{3.27}$$

Where V_f is the forward voltage drop across the diode and N is the multiplying factor and is equal to the number of diode-capacitor stages. It is clear that for each additional stage, another diode voltage drop gets subtracted. In reality, however, the magnitude of the DC output voltage will be smaller than in the previous equation because of the load sensitivity and non-linearity of diodes at low currents. Using a voltage multiplier can be beneficial for achieving a large enough voltage to effectively overcome the voltage barrier many DC-DC converters have; however, every increase in voltage demands a sacrifice in current and the power losses associated with the diodes can rapidly accumulate with increasing stages. For more comprehensive theory regarding these diode-capacitor voltage multipliers and charge-pumps refer to the extended theory in appendix A.

MOSFET Based Rectification

MOSFETs may also be utilised for rectification, the simplest method being diode-connected MOSFETS. However, like diodes, MOSFETS also require an input voltage above the device threshold voltage, which is typically significantly higher than Schottky diode forward voltage drops. When this threshold is surpassed, the output will experience a voltage drop equal to the MOSFET threshold voltage. Some simple rectifiers using diode-connected MOSFETS can be seen in figures 3.9A and B, these rectifiers are commonly used in RF energy harvesting. Figure A shows an NMOS only version, while B shows a CMOS version, using both positive and negative channel devices. The NMOS-only designs suffer from the body effect. which can lead to significant losses and is undesirable for ultra low-power applications. CMOS architectures (see figure 3.9) do not experience the body-effect losses; however, to counteract the lower mobility of holes in the p-channel compared to electrons in N-channel devices, the PMOS device should be chosen to have dimensions larger than those of the NMOS. However, these larger transistor dimensions lead to a larger parasitic capacitance C_p, incurring power losses. The threshold voltage requirement inherent to many MOSFET based rectifiers can be minimized by using so-called Self-V_{th}-Cancelling (SVC) techniques, such as in the comparator baseddesign shown in figure 3.9C. The rectifier shown in figure 3.9D is known as the 4 transistor cell /differential drive rectifier and is commonly employed in ultra-low power RF energy harvesters, by appending multiple stages of these cells the output voltage can be multiplied to higher values (reduced by the transistor threshold voltage).

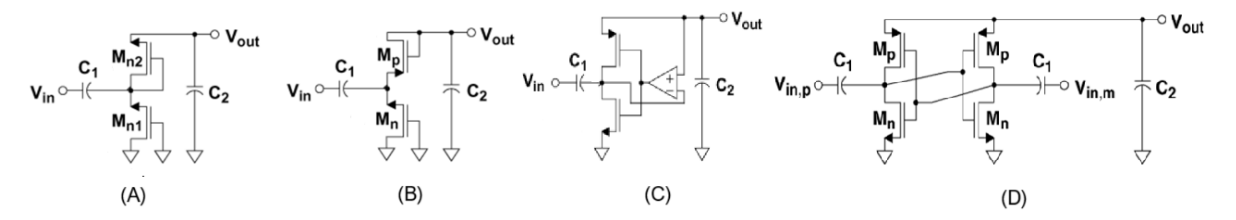


Figure 3.9: Various MOSFET-based rectifier topologies (A) NMOS-only diode-connected MOSFETs, (B) CMOS diode-connected MOSFETs, (C) Comparator-based rectifier, (D) 4 Transistor-cell differential drive rectifier. Adapted from [37].

Rectifiers based on designs C and D in Figure 3.9 were considered for their reported high efficiency at low power levels[37][13], but were abandoned due to the unavailability of ultra low-power comparators capable of reliable high-frequency switching and the absence of a center-tapped coil, which made the 4TC-DDR unfeasible.

To ensure a functional demonstrator within the limited timeframe, passive rectifiers were selected over MOSFET-based designs due to their relative simplicity and cost-effectiveness. However, in line with the modularity requirement, the rectifier in the prototype is implemented on a removable PCB, allowing for potential future upgrades or replacement with an active rectifier circuit.

3.2.2. PCE and Peak Power Simulations.

Power conversion efficiency (PCE) is a key performance metric when designing low-power rectifiers. It quantifies the ratio of output to input power and is critical for selecting an optimal rectifier topology. For diode based rectification the PCE can be approximated as:

$$PCE = \frac{P_{\text{out}}}{P_{\text{in}}} \cdot 100\% = \frac{P_{\text{out}}}{P_{\text{out}} + P_{\text{loss}}} \cdot 100\% \approx \frac{P_{\text{out}}}{P_{\text{out}} + (P_{\text{fwd}} + P_{\text{rev}})} \times 100\%$$
 (3.28)

Here P_{fwd} is the forward conduction power loss of the diode (primarily due to forward voltage drop) and P_{rev} is the power loss due to diode reverse leakage [13].

To determine the optimal diode choice, the power conversion efficiency (PCE) of an individual diode rectifier (essentially the HWR as pictured in figure 3.8A) was simulated in LTspice across different AC input voltages for various Schottky diode models under consideration. To isolate diode effects, all simulations used identical conditions: an ideal 36.48 kHz AC source, a 10 μ F output capacitor connected parallel to a 1 M Ω load resistor. This configuration resulted in microcurrents delivered to the load, reflecting the expected operating conditions for the system at large coil distances and high-impedance loads. PCE was determined by averaging the (steady-state) output DC voltage and load current and dividing it by the averaged input voltage-current product. Figure 3.10 shows the result of these simulations.

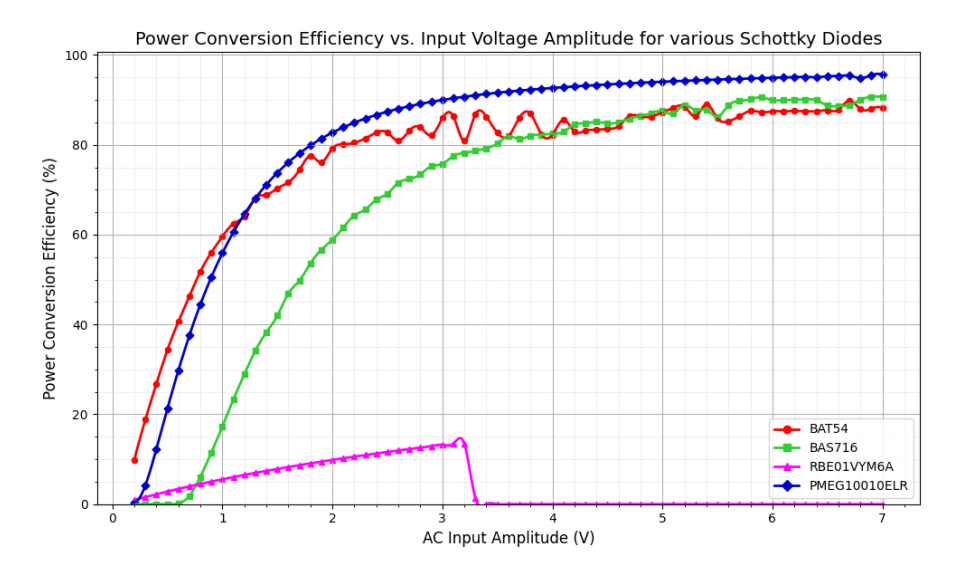


Figure 3.10: Comparison of simulated power conversion efficiency at various input voltages for different Schottky diodes in a half-wave rectifier configuration using LTspice.

From the results of these simulations it appears that the BAT54 Schottky diode is a slightly superior choice at sub-volt inputs, followed by the PMEG10010ELR. These two components significantly outperform the others. Despite having the lowest forward voltage by far (125mV), the RBE01VYM6A shows the poorest performance, likely due to its high reverse leakage and low breakdown voltage (6V).

Another important metric in assessing rectifier performance is peak power at the output of the rectifier. With calculated coupling factors and induced voltages the peak power over distance for was simulated using LTspice. The method used for calculating peak power makes use of the capacitor voltage-energy relation (refer to equation 3.33) to calculate change in stored energy over a time increment ($\Delta t = t_1 - t_2$):

$$P_{peak} = MAX(\frac{E_{t1} - E_{t2}}{\Lambda t})[W]$$
 (3.29)

The peak powers over coil distances were simulated for 2 different rectifier topologies and 3 different Schottky diodes; the BAT54, the PMEG10010ELR with a measured forward voltage of 330mV, and the RBE01VYM6A. Simulations were conducted using LTspice with a maximum timestep of 10 nanoseconds and an ideal rectifier output capacitor of 22 μ F.

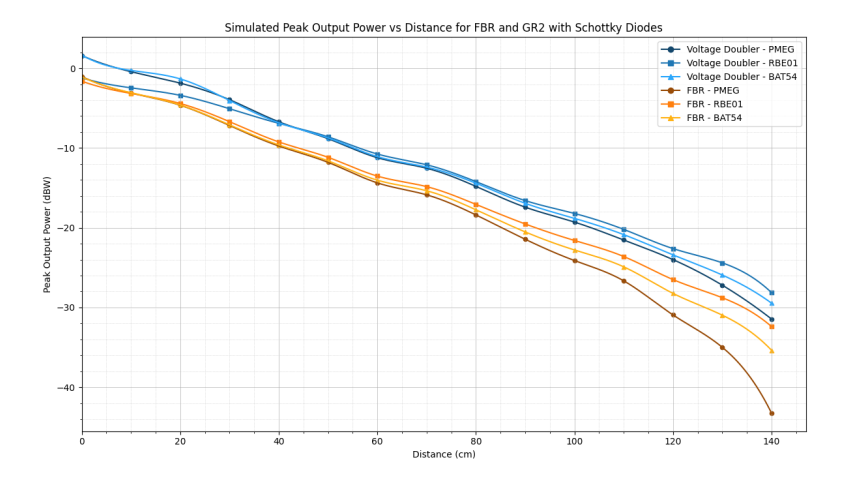


Figure 3.11: Comparison of simulated peak output powers over varying coil distance for 2 different rectifier topologies and 3 different Schottky diodes using LTspice.

The BAT54 has a higher maximum forward voltage, greater reverse leakage, and lower breakdown voltage than the PMEG10010ELR[16][18]. Considering these worst-case specs, along with the fact that subsequent DC-DC conversion will likely require minimum input voltages above 1 volt, where the PMEG10010ELR achieves a higher PCE, it was decided to use the PMEG10010ELR for the design of the device. In order to gain insight into the ideal rectifier topology using the PMEG10010ELR additional simulations were conducted for PCE and DC output voltage over distance. The simulations (shown in figures 3.11 and 3.12) imply that the GR2 is the ideal choice for balancing output voltage, peak power and PCE over distance.

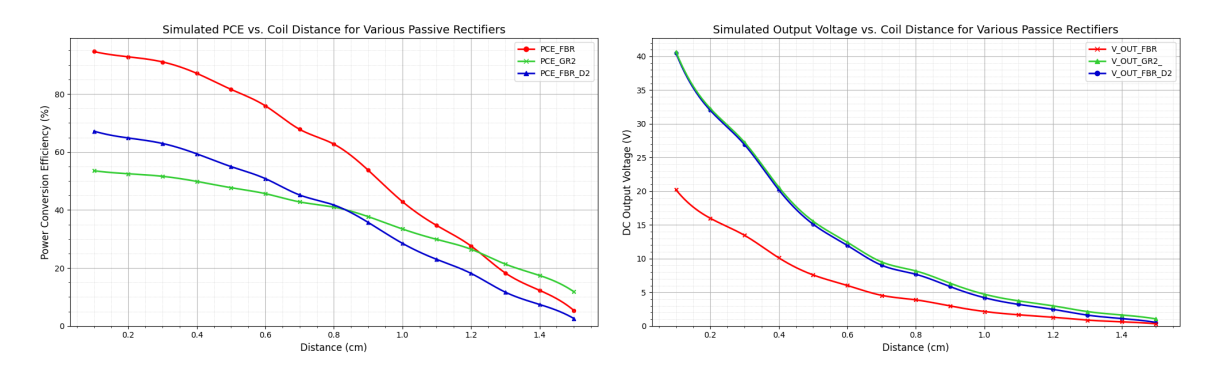


Figure 3.12: Simulated power conversion efficiency (PCE) (left) and DC output voltage (right) over Rx-Tx distances, for various passive rectifier technologies using PMEG10010ELR diodes. FBR_D2 denoting full-bridge rectifier followed by a 2 diode charge pump.

3.2.3. The Selected Rectifier Topology

From initial simulations it appears that the Greinacher voltage doubler outperforms the full-bridge rectifier in terms of peak power and PCE as shown in figures 3.11 and 3.12, however, as will be elaborated on in chapter 4, the FBR outperformed the GR2 in practice and was therefore selected as the rectifier topology of the prototype. The theoretical maximum output voltage of the FBR is given as:

$$V_{out} = V_{in} - 2 \cdot V_{fwd} \tag{3.30}$$

Although this rectifier configuration is capable of achieving a higher power conversion efficiency, the reduction of the output voltage by two times the forward voltage drop can be a detrimental limiting factor for the system performance.

Since many DC-DC converters have minimum input voltages above 1 volt, the resulting DC output might require additional boosting to reach a usable level. Fortunately, there are two possible approaches to boosting the voltage; a pre-boosting stage before rectification by means of a step-up transformer or post-rectification boosting of the DC signal by means of a diode-capacitor charge pump topology, as shown in Appendix Figure A.2. Although briefly investigated, charge pumps performed relatively poorly in practice and simulation (see figure 3.12). In order to comply with page limits, detailed theory regarding charge pumps and step-up transformers as well as simulations of pre- and post-rectification voltage boosting topologies are therefore omitted from the primary contents of this thesis, but can be found in appendix A and B.

3.2.4. Output Voltage Stabilization (DC-DC conversion).

From the mandatory requirement of a stable 2.1 Volt DC voltage over the MCU at a wide range of coil distances, it follows that robust voltage control is a necessity. In order to understand the choice of a buck-boost DC-DC converter, the nature of possible input signals must be understood. In the real-life use case, the Tx- and Rx-coils can be placed at a range of distances varying from 2.4 to 0 meters, these coil distances correspond to a wide input range as can be seen from figure 4.1. The MCU can operate from supply voltages ranging from 1.7V to 3.6V, in order to minimize power dissipation and power loss due to leakage it was opted to operate the MCU at a lower supply voltage of 2.1 V DC. Depending on the coil distances the estimated rectified voltage ranges from sub-volt levels to over 20 volt, meaning the output of the energy harvesting system should be able to step up input voltages below 2V and step-down input voltages above 2.1 V. A converter capable of both stepping up and down is thus required. Buck-boost converters require dedicated generated timing and switching circuitry, which can rapidly increase circuit complexity, fortunately many compact buck-boost integrated circuits (ICs) are commercially available at an affordable price. After extensive comparison of practical and financial feasibility of commercially available ICs and taking the program of requirements into consideration, the LTC3129 buck-boost converter manufactured by Analog Devices (formerly Linear Technology) was selected.

The LTC3129 buck-boost DC-DC converter is an ideal choice for attaining a stable output voltage due to the wide input range of 1.92V - 15V and adjustable output range from 1.4V to 15V, covering the entire range of the MCU's possible supply voltages. Furthermore, the I variant of the LTC3129 has a wide working temperature range of $-40C^{\circ}$ to $125C^{\circ}$, making it a perfect choice for the required operating range of the product. It also comes with a very low quiescent current of $1.3~\mu A$ and with a variety of power-saving features including maximum power point control, burst-mode operation and adjustable run voltage threshold [15].

Configuration and Optimization of the LTC3129

The LTC3129 has much of the complex circuitry on-chip, however, external circuitry is still required, particularly the inductor, capacitors and resistive voltage dividers to set-up the converter. The output voltage of the LTC3129 is adjustable by setting a resistive voltage divider over the feedback pin. the values for these resistors should be taken as large as possible in order to reduce leakage losses.

$$V_{OUT} = 1.175 \cdot (1 + \frac{R_1}{R_2}) \tag{3.31}$$

where R₁ connects V_{OUT} with the feedback pin and R₂ connects the feedback pin to ground. with $R_1=6.2M\Omega$ and $R_2=8.0M\Omega$, V_{OUT} is set at 2.086 V. By adding a potentiometer in series, this output voltage can be easily adjusted.

Next, the V_{cc} supply capacitor and switching capacitors must be chosen, according to the datasheet V_{cc} should be at least 2.2 μ F and for the two switching capacitors any value between 4.7 nF and 47 nF is recommended [15]. A low equivalent series resistance (ESR) is essential for minimizing capacitor losses in low-power applications, as such ceramic capacitors will be used in the prototype.

The inductor influences the maximum deliverable output current, ripple and overall efficiency. The DC series resistance of the inductor should be as small as possible in order to maximise output current and efficiency. For nearly all applications the ideal inductor is between 3.3 μ H to 10 μ H, with mostly bucking applications recommended to be on the higher side to reduce ripple and mostly boosting on the lower side. Since the output voltage is set slightly below the cold-start voltage, a value closer to 10 μ H is preferred. For the aforementioned reasons an inductor of 10 μ H (8.8 μ H measured) and 10 m Ω was selected.

Additionally, the LTC3129 also includes programmable RUN and MPPC pins. The run pin allows for the chip's internal circuitry to turn on at a user-set input voltage. allowing the converter to operate in 'hiccup' mode until the final output voltage is reached[15]. Details on how the chip was configured can be found in chapters 4 and 5.

3.2.5. Over-voltage Protection

The rectified output powers the buck–boost converter that stabilizes DC voltage despite coupling coefficient and load variations in the WPT link. However, the selected IC has a 15 V absolute maximum input rating, lower than the expected open-circuit coil voltages.

A 13 V Zener diode voltage clamp between the rectifier output node and ground can protect the converter from transient overvoltage events, in the event that the coils are placed very close to each other. Under normal operation (V < 13 V), the Zener remains non-conductive, presenting low leakage in the nano-amp range. During an overvoltage event, the Zener enters avalanche breakdown conduction, diverting excess energy to ground. This passive clamp limits the DC voltage to approximately 13 V, preventing converter damage or unintended shutdown. When selecting the Zener diode, particular attention was given to minimizing its reverse leakage current, as minimizing this parameter is key to minimizing power loss before breakdown. The diode selected for this is the BZX79-C13, with a maximum reverse leakage of 100nA [17], which is tolerable at the expected microamp current output of the rectifier.

Another important consideration in designing the overvoltage protection Zener clamp is power dissipation. Peak-power simulations using the rectifier (see Figure 3.11) estimate a worst-case peak power of under 2 W at the rectifier output (and thus the IC input). The selected Zener diode has a maximum power dissipation of 500 mW. Whilst the datasheet of the buck-boost converter does not explicitly state the maximum input power, an estimate can be made given the input voltage of 13 V and the (minimum) inductor current specification listed in the datasheet. With this information, a worst-case estimate for the converter's maximum input power is determined to be 2.86W at the programmed output voltage. This implies that the 500mW of power dissipation provided by a single Zener diode should be sufficient to protect the device.

Figure 3.15 shows the clamp's placement between the rectifier and buck–boost converter. The steep drop in load equivalent impedance at 13 V, observed in figure 3.13, represents the opening of a new conduction path parallel to the buck-boost IC, confirming this behaviour.

The robust power dissipation of the selected Zener device yields effective, low-component-count protection without appreciably affecting efficiency under nominal conditions.

3.2.6. Equivalent Input Impedance

To better understand the relationship between loaded and open-circuit voltage and facilitate potential future impedance matching, it is important to quantify the equivalent impedance of the system.

Estimating Equivalent Load Resistance at the Output of the Rectifier.

The MCU will be connected parallel to the capacitive energy storage, as illustrated in Figure 4.5.

Since the output of the buck-boost converter is DC with minimal ripple at steady-state ($t \to \infty$), the impedance of the capacitance approaches infinity and as a result can be approximated by an open circuit. leading to the following approximation for the equivalent impedance attached to the output of the buck-boost IC:

$$\lim_{t \to \infty} Z_{\text{eq}}(t) = \lim_{t \to \infty} Z_{C||MCU}(t) \approx R_{MCU}[\Omega]$$
(3.32)

The exact value of the MCU's equivalent resistance R_{MCU} varies greatly based on which functionalities are enabled in its programming and between idle and active cycles. Via idle current specifications and multi-meter measurements a resistance range between $2.4M\Omega$ and $6.7M\Omega$ was estimated. However, during simulation the MCU was modelled by a current draw of 1.1 μ A (specified MCU idle current draw + 20% safety margin).

The internal circuitry of the buck–boost IC is complex and varies greatly with operating conditions, making manual impedance calculation difficult. Fortunately, the LTC3129 is produced by Analog Devices and consequently has a built-in SPICE model in LTSpice. By simulating the input voltage and current under the MCU load at steady-state, the impedance behavior of the DC-DC converter can be analysed for varying inputs.

Figure 3.13 shows the simulated equivalent impedance of the buck-boost converter and MCU at steadystate. The sharp impedance drop starting at 13 volt can be attributed to reverse breakdown conduction of the Zener diode over-voltage protection.

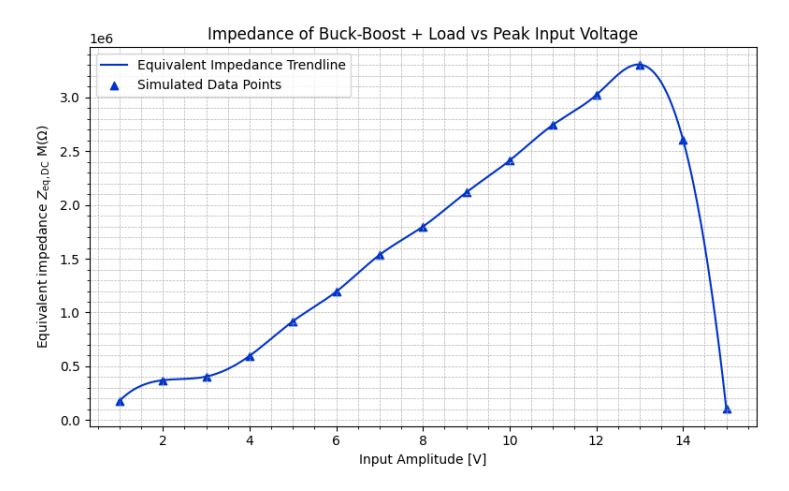


Figure 3.13: Simulated equivalent impedance seen at the output of the rectifier, including load, buck-boost, zener diode and ripple capacitor using LTspice. Sharp drop-off due to 13 V zener-diode reverse breakdown.

The Equivalent Input Impedance at the Rectifier

In designing for an eventual pre-boost step-up transformer (mentioned in Appendix A.1) the impedance behaviour of the entire system must be thoroughly understood. In figure 3.16 equivalent impedance as seen by at the input of rectifiers is displayed, the relative equilibrium between rising sections likely shows operation of the buck-boost converter, the drop in seen at close coil distances is likely due to the effect of the Zener voltage clamp.

Because performance at low input levels is crucial for long-range wireless power transfer, an eventual impedance matching network or step-up transformer should be tuned to the load impedance at low input conditions.

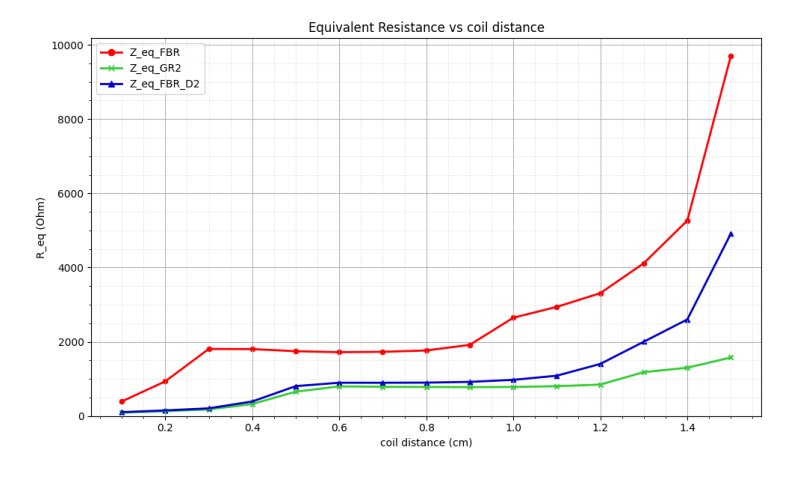


Figure 3.14: Simulated equivalent system impedance seen at the input of the rectifier, including load, buck-boost, zener diode and ripple capacitor using LTspice. FBR in red, FBR followed by 2 diode charge-pump in blue and Greinacher voltage doubler in green.

Based on measured Rx-coil DC resistance and the equations in section 3.1.3, the loaded input voltage will be closest to the the expected open-circuit voltages for the FBR, at the cost of sub-optimal power transfer.

3.2.7. The Proposed Rectifier - Circuit

Figure 3.15 presents an image of the proposed rectifier, including the Zener protection and buck-boost stages.

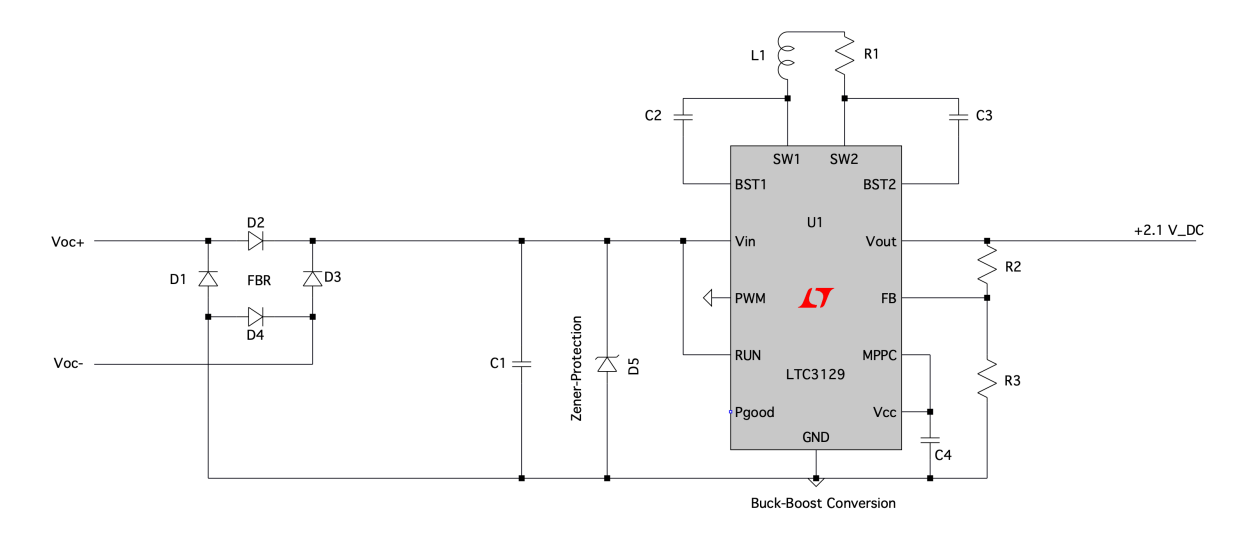


Figure 3.15: Visualisation of the proposed rectifier circuit, with subsequent stages attached.

3.3. Energy Storage

In this chapter, the energy storage of the system is analysed, beginning with an overview of the available storage options.

3.3.1. Energy Storage Options

Effective energy buffering mitigates the intermittent nature of magnetic energy transfer and transient load demands. Various storage technologies differ in energy density, charge/discharge behaviour, and practical constraints.

Electrochemical Batteries

Rechargeable batteries (Li-ion, NiMH, lead-acid) provide high energy density for long-term storage, but are hindered by cycle degradation, environmental concerns, and slow charging, making them unsuitable for applications requiring rapid energy capture. Moreover, since one of the mandatory PoR requirements prohibits battery usage, they are not a viable option.

Ceramic/Film Capacitors

Film and ceramic capacitors excel in fast charge/discharge for pulse buffering, thanks to low ESR and high cycle life. However, their low energy density makes them impractical for bulk energy storage.

Supercapacitors

Supercapacitors (typically electric double-layer capacitors) offer high power density and moderate energy storage, making them ideal for rapid energy bursts. However, their slow low-power charging, high self-discharge rates, and balancing circuitry requirements limit their effectiveness as a standalone solution for efficient energy transfer. Additionally, the PoR mandates that the system must start autonomously, which would take a significant amount of time if relying on supercapacitor storage.

Emerging Technologies

Thin-film microbatteries, solid-state electrolytics, and MEMS reservoirs offer compact energy solutions but are still in early development. Their high internal resistance and low energy capacity limit their viability for sustained-output applications. Additionally, their high cost contradicts the PoR requirement of budget adherence, making them impractical for this design.

Hybrid Approach

The design will adopt a dual-capacitor scheme: a microfarad-range ceramic capacitor near the buck-boost input buffers transients, while a larger bulk capacitor stabilizes long-term energy flow. This setup ensures low-impedance response to sudden load changes and voltage recovery, eliminating issues associated with battery waste, leakage, and charge time limitations.

3.3.2. Modelling (Super)capacitor non-idealities

At the expected microwatt received powers the non-ideal behavior of real-world capacitors becomes significant. To accurately capture these effects, supercapacitor models typically use parallel R-C networks. Higher complexity models, consisting of more R-C networks are generally more accurate at the expense of computational complexity [40]. The dominant losses stem from self-discharge (leakage) and equivalent series resistance (ESR), modeled by a parallel and series resistor, respectively. The equivalent circuit that will be used to approximate behaviour of non-ideal capacitors during the design process is shown in Figure 3.16.

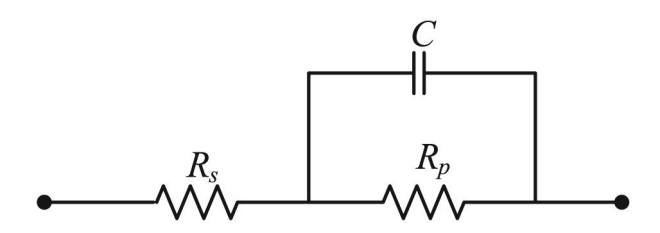


Figure 3.16: Equivalent capacitor model including ESR (R_s) and self-discharge (R_p) resistances as proposed by Spyker and Nelms [28], Figure adapted from [40]. Refer to Appendix D for equivalent circuit values relating to the prototype components.

3.3.3. Sizing the capacitors: Dual Capacitor Energy Storage

In order to postulate boundary values on the minimum output capacitance, 2 quantities related to the MCU are of utmost importance, these being the 'burst' energy required per active cycle measurement and the maximum acceptable voltage ripple. The first quantity was experimentally determined to be at most 20 μ J by the MCU subgroup [3]. The second quantity can be derived by considering the MCU's minimum supply voltage of 1.7 V in order to maintain its operating point and the target operating supply voltage of 2.1 V. Under these conditions, the absolute maximum permissible voltage ripple to maintain operation is calculated to be 0.4 V. By adding a safety margin of 100 mV above the absolute minimum supply voltage, a max ripple of 0.3 V is obtained.

Determining Burst and Storage Capacitors

A bound for the minimum capacitance of the burst capacitor can be calculated using the capacitor energy relation, as seen in Equation 3.33.

$$E = \frac{1}{2} \cdot C \cdot (V_{max}^2 - V_{min}^2) \quad [J]$$
 (3.33)

With the known values $V_{min}=1.8~{\rm V}$ (1.7 V with the 100mV safety margin), $E=E_{active}=20~{\rm \mu J}$ [3] and $V_{max}=2.1~{\rm V}$ (adjustable output voltage of buck-boost converter). The minimum bound for acceptable total output capacitance is given by Eq. 3.34:

$$C_{total} \ge \frac{2E_{active}}{(V_{max}^2 - V_{min}^2)} \approx 34.2 \quad [\mu F]$$
(3.34)

This implies a minimum output capacitance of 34.2 μ F to maintain proper operation. In order to maintain reliable operation at large spikes in current draw by the load (estimated peak 800 μ A during active cycle) as well as high power efficiency, the 'burst' capacitor used for the output must have leakage current and ESR as near to 0 as possible.

Ceramic X7R capacitors are a suitable choice due to their ultra-low leakage current and low ESR. Since ceramic capacitors are typically available only in lower capacitance values, multiple units can be placed in parallel to achieve the desired total capacitance. This parallel configuration also reduces the effective ESR, improving performance during transient spikes.

Adding an additional larger storage capacitor can further decrease voltage ripple and increase lifetime in energy scarce environments in the absence of a functional transmitter at the cost of increased leakage current and start-up time.

In addition to the 5 hour device operation lifetime in the absence of an energy beacon, as postulated in the PoR, required energies and minimum capacitances for other considered operational lifetimes are displayed in Table 3.3.

Where required energy stored is calculated via:

$$E = t \cdot P_{idle} + \frac{t}{3600} \cdot E_{active}[J]$$
(3.35)

| Time | Required Energy [μ J] | Required Capacitance [mF] |
|------------|----------------------------|---------------------------|
| 5 minutes | 633 | 1.08 |
| 15 minutes | 1895 | 3.24 |
| 1 hour | 7580 | 12.99 |
| 5 hours | 37900 | 64.79 |

Table 3.3: Required energies and minimum capacitances for considered operational lifetimes.

Unfortunately, properties that make a capacitor ideal for long-term storage tend to also limit the capacitor's capability of supplying short bursts of high current. In the output stage of a DC-DC converter, the capacitor must be large enough to maintain a stable DC voltage with minimal ripple, yet also have a low equivalent series resistance (ESR) to effectively handle high current spikes. A dual-capacitor energy storage scheme offers a practical solution by allowing each capacitor to be optimized for one of these functions.

3.3.4. The Start-Up and NFC Energy Harvesting Capabilities.

At distances near the device's maximum operating range, start-up issues may arise. This is primarily due to the MCU powering on with multiple peripheral functions enabled, leading to a substantial initial current draw. As the output capacitor reaches 1.7 V and the MCU activates, the resulting voltage drop can immediately shut it down, causing oscillatory on-off behaviour.

To address this, the NFC tag (connection point seen in figure 4.5) used for data retrieval also provides an energy harvesting functionality, capable of delivering peak power in the milliwatt range. This allows the system output voltage to be boosted to 3 volt within seconds, overcoming the start-up energy threshold [26].

It is important to note that this high current demand occurs only during the initial MCU active cycle. Furthermore, the system can cold-start without the NFC energy harvesting at the simulated distances. During testing, it was observed that the additional NFC energy boost enabled successful start-up beyond the simulated cold-start range, extending the maximum starting distance by approximately 10–20 cm.

4

Results

In this chapter, the theories and analyses from chapter 3 are applied to the design and construction of a prototype. The performance measurement results are then presented and analysed. Insights gained from the prototype are used to develop an approach for the final product.

4.1. Prototype Design and Implementation

Due to budget, time, and workspace constraints, recreating the actual deployment scenario was not feasible. Instead, a scale model prototype was developed in alignment with the PoR, providing similar functionality to the market-ready product but within a limited operational range.

4.1.1. Prototype - Energy Harvesting System

Using the theory discussed in Chapter 3.1.2, simulations were performed in LTspice. In the schematic presented in Appendix B.1.1, the mutual inductance and coupling factor were calculated for various distances, assuming near optimal alignment. Based on these results, Table 4.1 presents the component parameters utilised in the prototype energy harvester, representing the most optimal selections from these calculations.

| Component | Windings N | Radius [m] | Inductance [µH] | Parasitics (<i>R & C</i>) [Ω & pF] |
|--------------------------------|------------|------------|-----------------|--|
| Transmitter coil Receiver coil | 8 | 0.675 | 38.4 | 1.5 & 0.21 |
| | 305 | 0.11 | 55200 | 125 & - |

Table 4.1: The component parameters of the materials used to construct the transmit and receive coils for the prototype were analysed. Inductances were measured using an RLC meter and verified with Eq. 3.24 using a known frequency, voltage, and current. Parasitic resistance was also measured with an RLC meter and later verified using a multimeter. The parasitic capacitance of the Tx-coil was manually calculated based on the self-resonance frequency obtained from an impedance analyzer. The Tx- and Rx-coil parameters were chosen to match the ones theoretically calculated for figure 3.7.

Open-Circuit Voltage

Figure 4.1 (left) presents the simulation results, illustrating how the peak open-circuit voltage changes as the Tx-Rx distance increases. After completing the simulations, the actual components were assembled and arranged to replicate the simulated conditions in real life. The recorded practical open-circuit voltages are shown in Figure 4.1 (right).

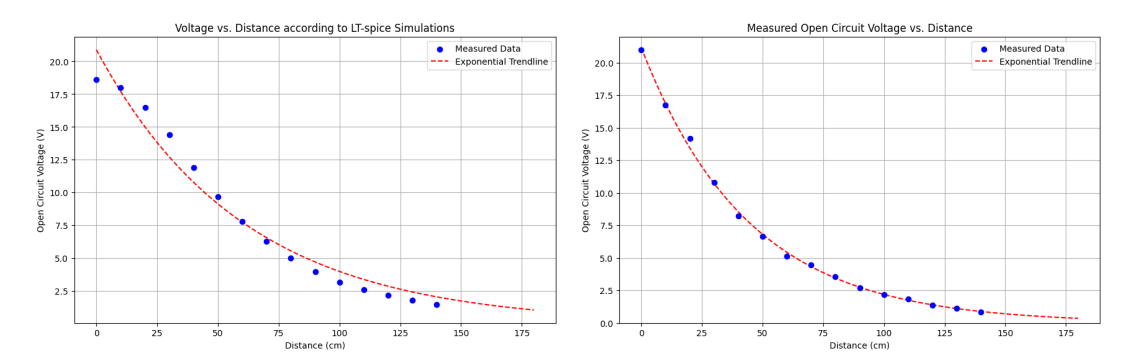


Figure 4.1: The left plot illustrates the relationship between open-circuit voltage and distance based on LTspice simulations. With the selected Tx-Rx combination and optimal alignment, a high open-circuit voltage is achieved at the output of the Rx coil. This plot was generated based on the results of the LTspice simulation of the schematic shown in 3.1.2. The right plot presents the experimentally measured open-circuit voltage versus distance, see Appendix B.1.1. While the practical values differ from the simulated results, the overall decay pattern remains relatively accurate.

In an ideal scenario, the voltage induced between wireless power transfer (WPT) coils would follow the inverse-square law, decreasing proportionally to $1/d^2$ as distance d increases, since the magnetic field B of the Tx coil is related to d ($B \propto 1/d^2$). However, according to the measurements, the voltage decay more closely resembles an exponential function, $1/e^d$, rather than the expected inverse-square trend. This discrepancy arises due to several influencing factors. Near-field effects dominate WPT systems, where inductive or resonant coupling causes a steeper voltage drop than simple electromagnetic wave propagation would predict. Additionally, resistive losses and eddy currents in real-world coils increase energy dissipation, accelerating voltage decay. Imperfect impedance matching between coils further reduces coupling efficiency, making energy transfer less effective than theoretical estimates. Environmental influences, such as dielectric materials and electromagnetic interference, also distort field propagation, exacerbating deviations from expected behaviour.

To mitigate these effects, resonant coupling is implemented using compensating capacitors on both Txand Rx-sides, enhancing energy transfer efficiency and maintaining a more stable voltage across varying distances.

Resonance Compensation and Alignment Testing

To optimize performance and power transfer between the coils, compensation capacitances were added, ensuring that both coils resonate at the same frequency as the source. These capacitances were calculated based on the resonance condition outlined in Eq. 3.16 and are presented in Table 4.2.

| Coil | Compensation Capacitor [nF] | | |
|-------------|-----------------------------|--|--|
| Transmitter | 500 | | |
| Receiver | 0.345 | | |

Table 4.2: The resonance compensation capacitances for the transmitter and receiver coils were calculated and implemented to increase performance.

The addition of compensation capacitors resulted in an increase of the open-circuit voltage by 1 to 2 volts compared to its original value, as shown in Figure 4.2 (left).

In addition to compensation adjustments, tests were conducted to observe the effects of misalignment between the receiver coil and the transmitter coil. The results of these alignment experiments, presented in Figure 4.2 (right), provide insight into performance variations due to angular offsets.

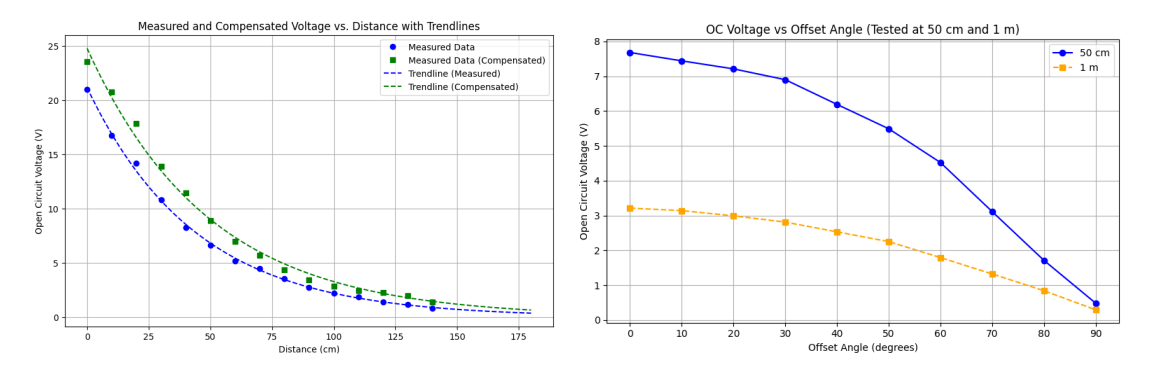


Figure 4.2: The left diagram illustrates the measured open-circuit voltage with and without added compensation capacitors. From the plots, it is evident that the compensation enhances the open-circuit voltage, resulting in an increase of up to 2 volts. The right diagram depicts the effects of misalignment between the transmitter (Tx) and receiver (Rx) coils. As the angle between Tx and Rx increases, a corresponding decrease in voltage is observed, which aligns with expected behaviour.

4.1.2. Prototype - Rectification, Output Stabilization and Energy Storage

Following the energy harvesting stage, a rectifier was built using PMEG10010ELR Schottky diodes, selected for their low forward voltage drop and improved efficiency, as discussed in the theory section. Both the GR2 and FBR were tested with a 10μ F ceramic capacitor, $2.7M\Omega$ resistive load and 13V zener attached to their outputs. Despite simulations presented in chapter 3.1, the FBR topology was preferred over the GR2 due to its superior performance, as demonstrated by the measurement results in Figure 4.3.

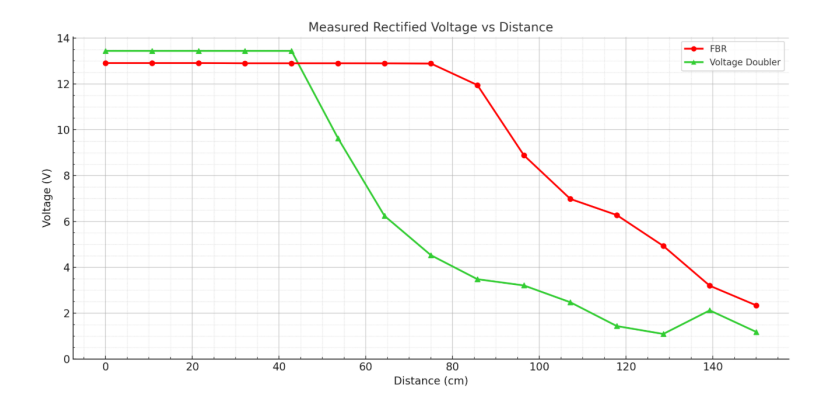


Figure 4.3: Measurement results comparing the full-bridge and voltage doubler rectifier topologies. The diagram demonstrates that the FBR achieves superior performance over larger distances, contrary to simulation results. Voltage clipping near 13V attributed to Zener diodes.

The FBR far outperformed its own simulated output voltage as seen in figure 3.12, while the GR2 resembled its simulated behaviour. Because of this deviation, the FBR measurement was conducted twice, with both tests leading to similar results. The exact reason for this large deviation is not fully understood, however possible resonance between the diodes' parasitic capacitance and Rx-coil inductance may provide an explanation for this discrepancy.

In line with the desired modularity of the subcomponents, the rectifier circuit was assembled on a removable PCB, facilitating disconnection from the rest of the circuit. Subsequently, the LTC3129 buck-boost converter was integrated according to section 3.2.4, with 6.8nF switching and $10\mu\text{F}$ supply capacitors. Alongside the 13V Zener diode over-voltage protection scheme, mentioned in the theory section, its input was connected to a $22\mu\text{F}$ electrolytic- parallel to $20\mu\text{F}$ ceramic capacitor enabling energy storage and robust current spike handling. MPPC and RUN functionalities were also tested, but the prototype performed better with these functionalities disabled.

For the energy storage capacitors of $50\mu\text{F}$ (ceramic X7R) and $3300\mu\text{F}$ (electrolytic) were used, providing a 15 minute lifetime in the absence of the beacon and an NFC-assisted start-up time of under 4 seconds [26]. A 6 hour energy reserve was initially desired as explained in the PoR (Chapter 2). However, implementing such a large capacitor without significantly impacting startup time was not feasible within the project timeframe.

Figure 4.4 illustrates the measured and simulated DC output across various coil distances for the assembled prototype. The output of the buck-boost converter stage was measured with the 50 μ F burst capacitor and a 2.7 M Ω resistive load connected to its output. The practical measurements closely matched the expected values, confirming both the functionality and validity of the implemented circuit design. Notably, the threshold distance at which the circuit begins operation and achieves the cold start voltage exceeded the simulations.

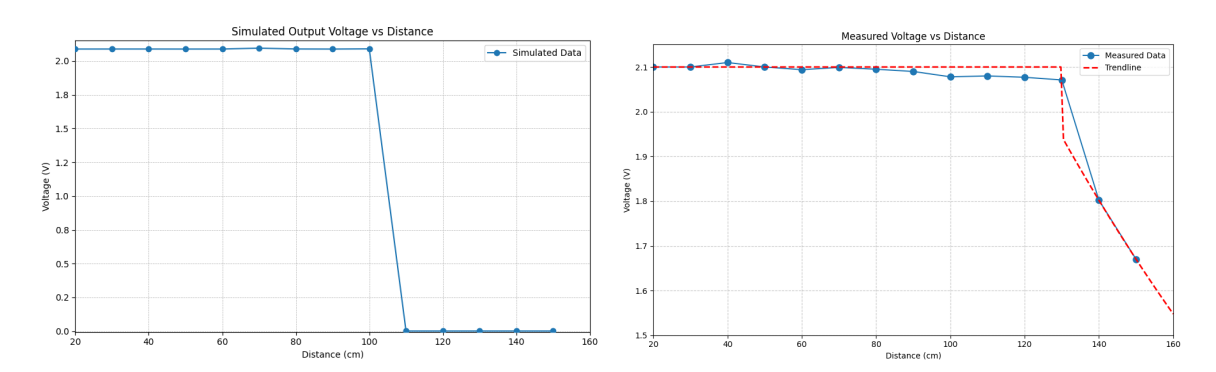


Figure 4.4: The left plot presents the simulated DC voltage at the output of the buck-boost converter for various Tx-Rx coil distances, obtained using LTspice. The right plot depicts the corresponding practical measurements. It is evident that the cold-start voltage of the buck-boost converter is reached at approximately 130 cm. Beyond this threshold, the system becomes operational and maintains a stable output of ±2.1 V. By comparing the two diagrams, it can be seen that the practical measurements outperforms the simulations.

4.1.3. Prototype - Final Design and Components

Figure 4.5 illustrates the circuit of the completed prototype. From left to right the sub-components are: Tx-Rx WPT coils, FBR, smoothing capacitor, Zener voltage protection, LTC3129 buck-boost converter with the aforementioned additional circuitry, 3.3mF storage- and 50μ F burst-capacitors, NFC harvested energy input and the MCU. As discussed earlier and further detailed in Chapter 6, the prototype satisfies the mandatory requirements outlined in the PoR.

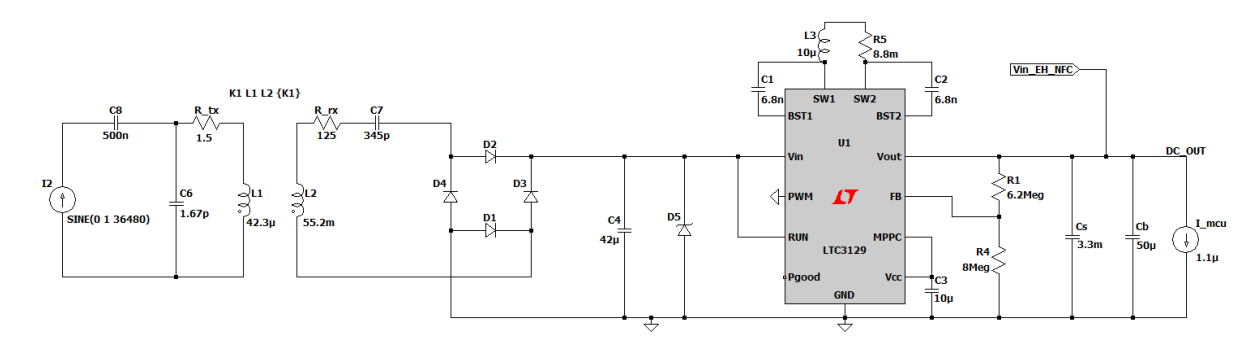


Figure 4.5: Circuit schematic of the complete energy-harvesting system (prototype). For a detailed component list, temperature tolerance list and capacitor specifications list, see Appendix D. For an image of the actual physical prototype, see Appendix B.2.

4.2. Designing for a Market Product

This section outlines the industrial-scale implementation of the batteryless inductive energy harvesting system, optimized for reliability, manufacturability, and compliance with maritime logistics constraints. In the PoR (Chapter 2) it is given that the final product must be operational at a coil distance of at least 2.4 meters, this distance is greater than the working range of the prototype. In order to extend the range to the 2.4 meter minimum outlined in the programme of requirements, some changes will have to be made in the design.

4.2.1. Market Product - Necessary Alterations

The biggest change between the designs of the prototype and market product lies in the inductive WPT link. The transmitter coil will be powered by an industrial-grade resonant inverter, replacing the EDU33212A function generator and TS400 amplifier.

In order to boost the received voltage to useable level, it operates at a fixed current drive of 3 A instead of 1 A, and with a frequency of 50 kHz. The design adheres to EU directive 2013/35/EU, ensuring field strength remains \leq 100 μ T.

Modifications to Transmitter Coil

Geometrically, the transmitter coil is a rectangular loop that spans the perimeter of the container ceiling, optimizing coverage within the 6.0×2.4 m dimensions. However, in order to simplify estimation, the induced field of this rectangular coil will be approximated by 2 circular loops of 2.4 meter diameter, as shown in Appendix A.3. Taking the theory outlined in Section 3.1 as a foundation and working backward from Equation 3.5, it can be shown that for Rx-coil properties similar to those of the prototype (see Table 4.1), a theoretical open-circuit voltage of 3.64 V is attainable at 2.4 meter for a magnetic flux density of $B_{Tx}(2.4) = 1$ μ T and a frequency of 50 kHz (under perfect alignment). Based on equation 3.2, such a flux density value can be achieved if the product $N_{Tx} \cdot I_{Tx}$ satisfies:

$$N_{Tx} \cdot I_{Tx} \ge 10.804 \tag{4.1}$$

Since coupling factor is inversely proportional to the root of the self-inductance, and the self inductance is proportional to the square of the number of windings, a lower winding count and higher current is desired. A configuration of $N_{Tx} = 4$, $I_{Tx} = 3$ A was adopted. Assuming a wire gauge similar to that of the audio wire/ speaker cable that was used in the prototype's beacon (t \approx 1 mm, this also helps with keeping costs low) the inductance of a single turn of the aforementioned diameter can be estimated using equation 3.9 by[24]:

$$L = \mu \cdot d(\ln(\frac{8d}{t} - 2))[H] \tag{4.2}$$

Where $\mu = \mu_r \mu_0$, d is loop diameter and t is wire thickness.

Since

$$L \propto N^2 \tag{4.3}$$

Using the aforementioned equations and values leads to a calculated self inductance of $L_{Tx} \approx 456.3~\mu\text{H}$. Via equations 3.7 and 3.8, coupling coefficients for the new Tx-coil and the prototype Rx-coil were calculated at distances spanning 0 to 3.0 meter in 0.1 meter increments. The found coupling coefficients were then used to simulate the WPT link in LTspice, the results of the simulated induced open-circuit voltage can be seen in figure 4.6 (left).

System Performance of the Market Product

The remainder of the system, shown in Figure 4.5, was connected to the simulated WPT link using the calculated k values. The buck-boost converter's output over distance was then simulated for the updated Tx-coil and frequency in LTspice. The results are presented in Figure 4.6 (right), with the 3.3mF storage capacitor omitted to reduce simulation time.

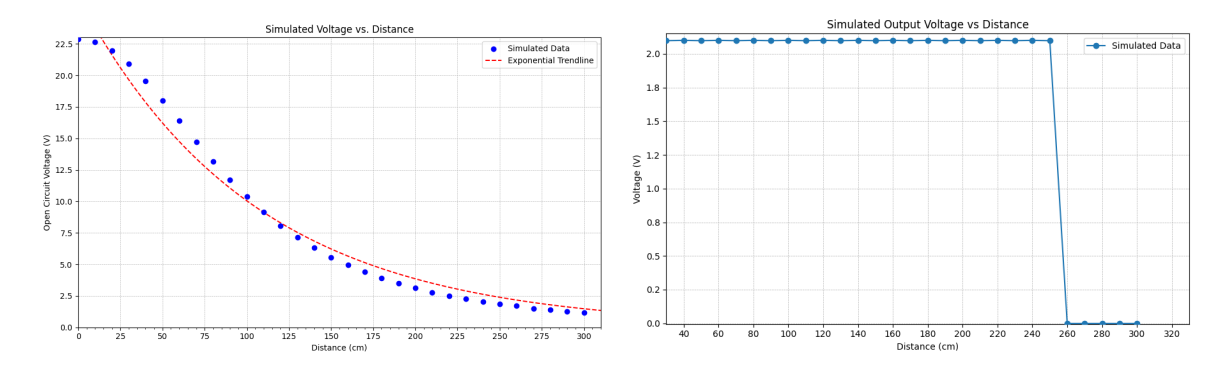


Figure 4.6: Induced open-circuit voltage over distance for estimated coupling coefficients, simulated using LTspice (left). Simulated DC output voltages for various Tx-Rx coil distances(right), obtained using LTspice. It is evident that the cold start is achieved at distances of 250 cm or less, satisfying the mandatory minimum operating distance requirement postulated in Chapter 2.

4.2.2. Market Product - Validation of the Coil Approximation Method

Since no physical coil is available for testing, the expected performance of the market product was estimated. To validate the accuracy of the circular coil approximation, the Biot–Savart law (as introduced in Equation 3.1) is adapted for four straight segments forming a rectangle with dimensions similar to the container. Multiplying the sum of the segments by the number of windings allows estimation of the magnetic flux density at the centre of the rectangular coil. By comparing this result to the corresponding value for a circular approximation (assuming uniform fields), the validity of the circular model can be assessed.

Magnetic flux density at the centre of the rectangular coil with 4 windings carrying 3 A:

$$|B_{Tx}| \approx 4 \cdot |2 \cdot B_{6m}(1.2) + 2 \cdot B_{2.4m}(3)| \approx 4 \cdot |1 \cdot 10^{-6} + 4 \cdot 10^{-7}| = 5.6 \,\mu\text{T}$$
 (4.4)

Where r is distance to the line segments, $B_{2.4m}$ and B_{6m} are magnetic flux density contributions of the 2.4 m and 6 m line segments respectively.

The magnetic flux density at the centre of the circular loop approximation with 4 windings (taken from equation 3.2):

$$|B_{Tx}(0)| \approx 6.28 \,\mu T$$
 (4.5)

This is a rough approximation that neglects fringing effects and assumes a uniform magnetic field.

Due to the limited number of turns, the deviation between magnetic flux density magnitudes remains minimal. Furthermore, since magnetic flux density is maximal at the center of the coils, both Tx-coils comply with Directive 2013/35/EU (B < $100 \,\mu$ T) and even meet the public exposure guideline (B < $6.25 \,\mu$ T) beyond $10 \,\mathrm{cm}$.

The rectangular coil has a single-turn inductance of approximately 24.8 μ H, as derived in Appendix A.3. Using relation 4.3, the inductance for a 4-turn version is estimated at $L \approx 396.8 \mu$ H. Although slightly lower than the circular approximation (456.3 μ H), it shouldn't negatively affect performance, on the contrary, the reduced self-inductance may improve coupling coefficients, as suggested by equation 3.8.

4.2.3. Market Product - Misalignment Prevention

An additional feature for the market-ready product is enhanced misalignment prevention compared to prototype, with several possible solutions:

- One approach is to add a second or third beacon coil orthogonal to the ceiling-mounted coil. This configuration would ensure proper alignment regardless of the Rx-coil's orientation.
- Another option, which could deployed in case of a budget limitation, is integrating insertion slots into the crates, allowing the product to be placed securely in a designated slot, ensuring perfect alignment with the beacon.

4.2.4. Modifications to the Rest of the System

Thus far, the only changes between the prototype and the final product are in the Tx-coil, with the entire Rx-coil and rest of the prototype unchanged. Simulations using the updated Tx-coil demonstrate that the original prototype is capable of cold-starting at the minimum distance of 2.4 meters (Figure 4.6). Hence, no changes are required in the rectifier and buck-boost converter.

In order to assess the robustness of the prototype's overvoltage protection for the altered Tx-coil, the peak power was simulated for the updated WPT link's induced voltages according to the method outlined in section 3.2.2. A peak power of 948 mW was recorded at a coil separation of 0 cm, indicating that the prototype's single Zener diode clamp effectively protects the LTC3129 under the worst-case conditions outlined in section 3.2.5.

Discussion

Experimental validation confirmed theoretical analyses of the energy harvesting coil, rectification, protection, and output stabilization. The system achieved a stable 2.1 V DC output at over 2.1 µW (inferred by the turn-on behaviour of the MCU), without batteries or pre-charged capacitors—directly tackling e-waste from conventional sensors in logistics.

5.1. Key (Experimental) Findings

• Energy Harvesting Performance

The prototype reliably harvested energy from an inductively coupled beacon at up to 1.4 m separation. Though below the 2.4 m target, simulations suggest an optimised beacon coil (larger diameter, higher current, and fewer windings) can achieve the required range. The observed exponential decay in open-circuit voltage, deviating from the theoretical inverse-square law, highlights practical challenges like near-field effects, resistive losses, eddy currents, and impedance mismatches. Compensation capacitors significantly improved voltage, emphasizing the role of resonance matching in efficient power transfer.

Rectification and Voltage Stabilization

Contrary to simulation results in Figures 3.12 and 3.11, the full-bridge rectifier topology with PMEG10010-ELR Schottky diodes outperformed the Greinacher voltage doubler in practice, as can be seen from figure 4.3. The exact reason for this discrepancy is not fully understood, and requires additional testing.

As shown in Figure 4.4, the LTC3129 buck-boost converter stabilized the output at 2.1 V across varying inputs, achieving cold-start operation at 130 cm without external initiation from the NFC energy harvesting. The Zener diode clamp effectively protected sensitive components from high voltages at close coil proximities.

Energy Storage

Although the 5-hour energy storage Trade-off requirement could not be met without significantly compromising startup time, a 3.3 mF capacitance was feasible leading to a theoretical maximal beacon-free operation of 15 minutes and NFC-assisted start up time of under 4 seconds[3]. The dual-capacitor energy storage scheme effectively addressed the intermittent nature of energy harvesting and the burst power demands of the MCU. This approach avoids the drawbacks of batteries (e-waste and maintenance), contributing to the system's required "set-and-forget" usage model.

Market Product Design Considerations

The transition from prototype to market product involves scaling the transmitter coil to fit container dimensions and adjusting parameters for a fixed current drive of 3 A at 50 kHz, while adhering to EU magnetic field strength limits. The approximation of the rectangular container coil with circular loops for simulation purposes provided a reasonable estimate of performance, suggesting that the 2.4 m operational range is achievable. Considering that the prototype outperformed simulated cold-start distances and given the observed benefits of the NFC energy harvesting capability, the final product could potentially start at distances exceeding 2.5 meters in practice.

5.2. Limitations and Trade-offs

Prototype Distance Limitation

The prototype's operational range of 1.4 meters, while sufficient for the demonstration, necessitates further optimisation of the beacon for the 2.4-meter target in a full-scale container. Comprehensive large-scale physical testing at this distance was infeasible within the project scope, thus this meant relying on theory and simulations for the market product.

Coil Approximation Inaccuracies

The use of circular coil approximations for the rectangular, container-spanning transmitter coil, while simplifying analysis, introduces minor inaccuracies in the theoretical predictions. Real-world performance may exhibit slight deviations due to fringing effects and non-uniform magnetic fields not fully captured by these ideal approximations.

Diode Choice Justification

According to the theory section, the BAT54 diodes showed slightly higher efficiency at sub-volt inputs. However, their datasheet indicates that this comes at the cost of a 13-fold increase in reverse leakage current and a slightly higher maximum forward voltage[16][18]. Therefore, the chosen PMEG diode appeared to be the optimal choice. Later simulations of the complete system appear to support this choice (see Appendix Figure B.3).

Low-Input Efficiency Challenges

Maintaining high power conversion efficiency at very low input voltages remains an inherent challenge for passive rectification circuits. This could potentially limit the system's performance at the extreme ends of the 2.4-meter operational distance. Although not realisable within the project timeframe, fututure implementation of an active rectifier using V_{th} cancelling techniques could lead to improved system performance and overall efficiency.

Supercapacitor Self-Discharge

Although the dual-capacitor system effectively mitigates many issues, the inherent self-discharge of supercapacitors, even those with low leakage currents, will ultimately impose a finite limit on the "maintenance-free" operational duration in the complete absence of a functioning beacon.

5.3. Lessons Learned

• The Influence of Resonance Matching

The significant improvement in open-circuit voltage observed with the addition of compensation capacitors decisively demonstrated that precise resonance matching is an important factor for achieving efficient wireless power transfer, especially over larger distances.

· Practical vs. Theoretical Decay Results

The notable discrepancy between the theoretical inverse-cube voltage decay and the empirically observed exponential decay in real-world setups underscored the complexity of near-field interactions and highlighted the critical importance of empirical validation alongside theoretical modelling.

Value of Comprehensive Performance Metrics

Relying on a single performance metric can lead to misleading conclusions. For instance, while the RBE01VYM6A diode showed strong results in peak power simulations, its poor PCE revealed significant performance limitations (section 3.2.2). This highlights the need to assess performance across multiple metrics, but simultaneously validate simulation results through real-world testing, as simulations can also be deceiving.

Low-Power Component Selection

The choice of components, such as ultra-low forward voltage Schottky diodes, the low-leakage Zener diode and the LTC3129 buck-boost converter with its low quiescent current, was undeniably vital for enabling the system's self-starting capabilities and ensuring efficient operation at very low power levels.



Conclusion

This thesis presented the successful design, implementation, and evaluation of a batteryless inductive energy harvesting system intended for wireless temperature sensing in shipping containers. The proposed design presents a relatively sustainable and low-maintenance alternative to battery-powered sensors, contributing significantly to the reduction of e-waste, without compromising on the accuracy and effectiveness of condition monitoring data loggers. The prototype met all mandatory requirements as outlined in chapter 2. The developed prototype:

- Achieved a stable DC output voltage of at least 2.1 V at an average power greater than 2.1 μW.
- Operated without any battery or pre-charged energy storage.
- Functions reliably over the required operating temperature range (see appendix D).
- · Was entirely powered by inductively harvested energy.
- Has the ability to operate maintenance-free for an extended period of time.
- Maintained functionality over a coil separation distance of up to 1.4 m, with theoretical expansion up to 2.4 m based on simulations using the appropriate beacon.
- Complied with the legal magnetic flux density limit of 100 µT, whith the market product likely even meeting the recommended public safety limit of 6.25 µT at distances beyond 10 cm.
- Stayed within the budget constraint of €70 for the prototype.
- Required no structural modification or mounting on the container exterior.

Additionally, simulation results demonstrated that the prototype (with further refinement of the beacon) can operate at the same 2.4 meter distance required for the final product, suggesting a feasible path toward commercialization. The integration of resonance matching and the use of a dual-capacitor energy storage design significantly improved both energy transfer efficiency and system robustness under realistic operating conditions.

Future Work

While the prototype successfully meets all defined goals, several opportunities remain for future research and development. Enhancing the beacon coil design could improve efficiency and reduce electromagnetic interference, ensuring stable energy delivery across greater distances or through materials with varying permeability.

Additionally, integrating energy-aware scheduling algorithms would help extend operational duration during beacon outages, making the system more resilient. Further advancements in miniaturization and modularity could enhance deployment flexibility while lowering production costs.

Finally, field testing under real-world logistics conditions would provide valuable insights into long-term reliability, misalignment tolerance, and resistance to mechanical vibration or RF noise.



Appendix A - Extended Theory

A.1. Energy Harvester - Further Compensation Methods

In case the desired voltage, at the output of the receiver coil, over the load cannot be obtained, compensation can be done in one of several forms:

- Using an *L-network* to match the impedances of the Rx-coil and the load.
- Adding a step-up transformer between the Rx-coil and the load with the proper winding ratio.
- · Utilizing active matching through e.g. a transimpedance amplifier or a MOSFET cascade buffer.

L-Network

The implementation of an impedance matching L-network, as presented in [29], requires adding an inductor in series and a capacitor in parallel with the load. The component values are determined by first calculating the loaded quality factor:

$$Q = \sqrt{\frac{R_L}{R_{S2}} - 1} \tag{A.1}$$

Yielding the component values:

$$L_{series} = \frac{Q \cdot R_{s2}}{2\pi \cdot f} \tag{A.2}$$

$$C_{parallel} = \frac{1}{2\pi \cdot f \cdot \frac{R_L}{O}} \tag{A.3}$$

While large R_L/R_{s2} mismatches could theoretically be addressed with this approach, the L-network behaves as a near-short circuit at resonance. This results in prohibitive current losses that fundamentally undermine efficiency in a power-constrained system. Additionally, the requisite component values would be physically impractical given the operational constraints.

Step-up Transformer

A step-up transformer, as mentioned in [6] (pages 1754-1765), with appropriate turns ratio provides a more viable passive solution. The transformer consists of two inductors magnetically coupled with near-perfect coupling ($k \approx 1$). The turns ratio is governed by:

$$\frac{N_p}{N_s} = \frac{V_p}{V_L} \tag{A.4}$$

where N_p/N_s are primary/secondary windings and V_p/V_L are primary/load voltages. The inductance relationship follows:

$$\frac{L_p}{L_s} = \left(\frac{N_p}{N_s}\right)^2 \tag{A.5}$$

Critical design requirement: $X_{Lp} > R_{ref} = R_L (N_p/N_s)^2$ where X_{Lp} is primary reactance and R_{ref} is reflected impedance.

Active Matching

Active solutions require dedicated power supplies for amplification stages. Since our system lacks provision for auxiliary power and must operate as a fully passive energy harvesting circuit, these techniques are fundamentally incompatible with our architecture.

Combined System Model

Among the three options, the step-up transformer emerges as the only feasible solution, providing necessary voltage gain without external power or prohibitive current losses.

With the incorporation of the transformer, the fully compensated circuit is depicted in Figure A.1.

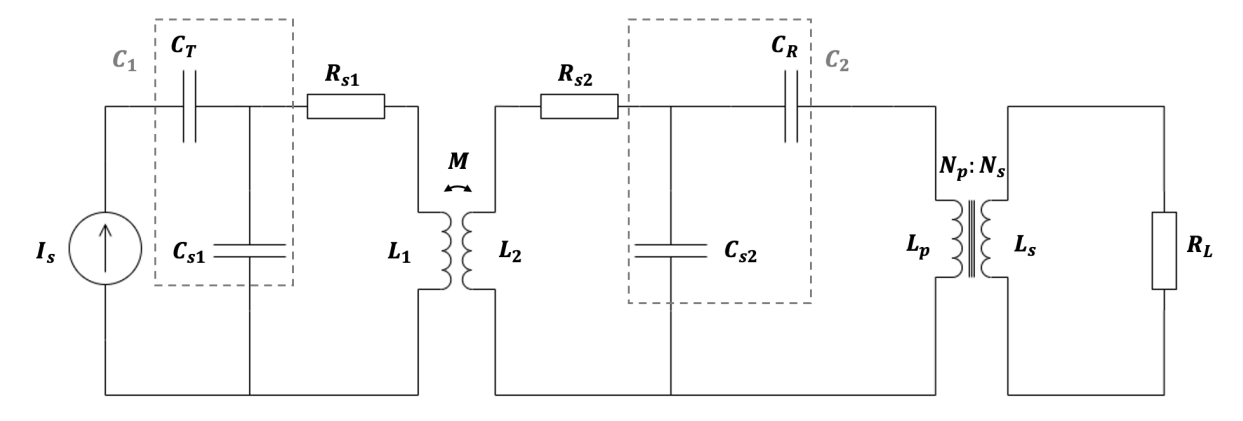


Figure A.1: The Tx-Rx circuit, as shown in Figure 3.3, includes added compensation. The source is modeled as a current source without internal impedance, since this is canceled by the amplifier.

The components in Figure A.1 are largely identical to those in Figure 3.3, with the addition of I_s , L_p and L_s , which represent the source current after amplification, the primary inductance, and the secondary inductance of the transformer, respectively.

A.2. Rectifier - Discussion of Additional Topologies and Voltage Boosting Methods

A.2.1. Passive DC Voltage Boosting: Diode Charge Pumps.

It is clear that 3 primary parameters need to be selected for in order to achieve a desired charge pump performance, these being number of stages N, the capacitances C and the operating frequency f. Since the charge pump will be driven from the AC voltage of the harvested inductive energy the frequency is given and equal to the value derived in chapter 3.1.

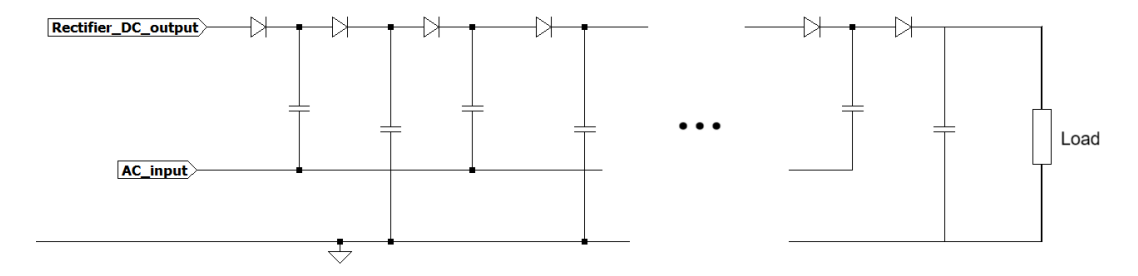


Figure A.2: Schematic of single phase input-driven diode-based Dickson charge pump, '...' denoting additional stages.

For maximizing the power efficiency the value of the unloaded output voltage V_0 should be twice as large as the desired loaded voltage

Under this condition the number of stages is given as:

$$N = 2\left(\frac{V_0}{U_{EH} - V_{fwd}} - 1\right)[-] \tag{A.6}$$

The Capacitances used for each stage should comply with the condition

$$C > \frac{N}{f \cdot F \cdot (N+1)^2 \cdot R_{EH}} [F] \tag{A.7}$$

where F is the cresst factor and R_{EH} the equivalent impedance of the rectifier.

using equations A.24 with the forward voltage drops of the shottky diodes, we calculate F to be equal to

$$F \approx 1.59 \tag{A.8}$$

$$C > \frac{5}{36.48kHz \cdot F \cdot (6)^2 \cdot R_{FH}} [F]$$
 (A.9)

In modelling power transfer the Dickson charge pump can be approximated by a DC voltage source followed by an equivalent resistance [31], the values of which can be determined by:

$$V_{0,\text{TANZAWA MODEL}} = (N+1) \cdot (V_{EH} - V_{th}) \text{ [V]}$$
(A.10)

$$R_{S,\text{TANZAWA_MODEL}} = (N+1)^2 R_{EH} + \frac{N}{f \cdot C} [\Omega]$$
 (A.11)

Where R_{EH} is the DC output of the energy harvester, in the proposed energy harvester this value is equal to the DC output of the rectifier.

The equivalent impedance of an N-stage Dickson charge pump can be found according to the formula[[36]]:

$$R_{\rm eq} = \frac{N}{fC} + F(N+1)^2 R_{EH}$$
 (A.12)

Where N is the number of stages, f is operating frequency, C is the capacitance used in each stage, F is the crest factor and R_{EH} is the input impedance (impedance of the FBR).

In theory the crest factor F can be expressed as the peak voltage or current value divided by their RMS value, which would equal $\sqrt{2}$ for a sinusoidal input, however in practice there are 4 so-called "dead" times in each period of the sinusoidal input, which are caused by the forward voltage drop the diode requires before conducting, this effectively lowers the RMS value and leads to a higher F factor[[36]]. Taking into account the dead times the crest factor can be expressed as:

$$T_{\text{dead}} = \frac{\arcsin\left(\frac{V_{\text{fwd}}}{V_{\text{EH}}}\right)}{2\pi} \cdot T[s] \tag{A.13}$$

now with the found dead-time, the duty cycle of the switching diodes is equal to:

$$D = 1 - 4 \cdot \frac{T_{\text{dead}}}{T} \tag{A.14}$$

And then finally the crest factor is given by:

$$F \approx \frac{\sqrt{2}}{D} \tag{A.15}$$

From this the driving current at the output of the charge pump can be found:

$$I_{\mathsf{EH_MAX}} = \frac{1}{F} \frac{V_{\mathsf{EH}} - V_{\mathsf{th}}}{R_{\mathsf{EH}}} [A] \tag{A.16}$$

The output current of an N-stage charge pump:

$$I_{OUT} = \frac{I_{IN}}{N+1} [A] \tag{A.17}$$

putting equations A.16 and A.17 together we can derive an upperbound for the output current of the charge pump:

$$I_{OUT_{MAX}} = \frac{1}{F \cdot (N+1) \cdot R_{EH}} \cdot (V_{EH} - V_{th}) [A]$$
 (A.18)

The output voltage of the charge pump can never exceed DC voltage of the source in the equivalent model:

$$V_{OUT_{MAX}} = V_0 = (N+1) \cdot (V_{EH} - V_{th}) [V]$$
(A.19)

Applying Ohm's Law:

$$R_S = F \cdot (N+1)^2 \cdot R_{EH} \left[\Omega\right] \tag{A.20}$$

Then, by combining A.11 and A.20 the equivalent Impedance of the charge pump can be expressed as:

$$R_{S_{EH}} = F \cdot (N+1)^2 \cdot R_{EH} + \frac{N}{f \cdot C} \left[\Omega\right]$$
 (A.21)

Then taking into account the number of stages, the forward voltage drop of the diodes and their parasitic capacitances we arrive at the theoretical output voltage of an N-stage Dickson charge pump[36]:

$$V_{0_EH} = (N+1) \left(\frac{V_{EH}}{\sqrt{R_{EH}^2 \omega^2 C_{PAR}^2 + 1}} - V_{fwd} \right) [V].$$
 (A.22)

Simulation results of equivalent impedance seen from output of compensating network (Including the load, storage capacitors, buck-boost IC, 2 diode charge pump(blue), or greinacher voltage doubler(green) and FBR can be seen in figure 3.16.

A.2.2. Voltage Multiplying Rectifiers

As shown in figure 3.8, there are 2 capacitors in the voltage doubler, the primary input capacitance C1 and the ripple/output capacitor C2. The latter sets a boundary on the acceptable output voltage ripple of the doubler. Since the Greinacher circuit is a simple voltage doubler of N = 1 the theoretic maximum output voltage is given by

$$V_{OUT,DC} = 2(V_m - V_{fwd}) = [V]$$
 (A.23)

Where V_m is the amplitude of the input voltage, V_{fwd} the forward voltage drop across the diodes.

For a kHz frequency, micro amperes and a voltage ripple of a few millivolt the required capacitance is in the nano Farad range. There is no hard rule for the value of C1, but in order to improve charge transfer it should generally be equal or larger than C2.

The exact impedance of a voltage multiplier is a time varying value, but an effective impedance value for a voltage multiplier of N stages can be approximated by:

$$Z_{\text{out}} = \frac{N(N+1)}{2fC} \tag{A.24}$$

Where f is frequency, C is capacitance and N is number of stages.

This value considers ideal components, a more accurate expression takes diode dynamic resistance and capacitor's equivalent series resistance into account as well. The losses in the Greinacher voltage doubler are given by:

$$Z_{eq} = (R_{ESR} - \frac{1}{fC}j) + R_d$$
 (A.25)

 R_d in equation A.25 is the diode dynamic resistance and is equal to the forward voltage-current curve, $R_d = \frac{\Delta V_{fwd}}{\Delta I_d}$ and is non-linear.

The diodes in the voltage multiplier and Dickson pump also contribute to the overall equivalent impedance. In passive rectifiers the equivalent diode impedance depends on various factors such as the frequency, the forward and reverse voltage drops of the diode. The DC resistance of a forward-biased diode can be calculated by applying Ohm's law:

$$R_d = \frac{V_f}{I} \tag{A.26}$$

Where V_f and I_f denote the forward voltage drop and the current through the diode respectively.

However, the impedance of a diode is not constant and varies with changing applied voltages. Under a time-varying voltage the current of through diode also changes with time. The dynamic resistance of a diode if the I-V curve of a diode is known the AC or dynamic resistance can be estimated by:

In reality, capacitor impedance is also affected by equivalent series resistance (ESR) and parasiticinductances. A more accurate expression of capacitance impedance would be:

$$Z_{cap} = \frac{1}{j\omega C} + j\omega L_p + R_{ESR}$$
 (A.27)

Luckily, the effect of parasitic inductance is minor at low frequencies (under 100kHz) and especially in devices in small pacakages (like the X7R ceramic capacitors intended for the rectifier). Furthermore, the effect equivalent series resistance is significantly lowered by selecting capacitors of this type, which have typical ESR values between 0.01Ω and 0.1Ω .

If initial rectification is achieved using a voltage doubler and its output is boosted by N charge pump stages, the equation for the equivalent impedance of the voltage doubler including the charge pump can be approximated by:

$$R_{\text{eq}} = \frac{N}{f \cdot C} + F(N+1)^2 \frac{1}{f \cdot C_{CW}}$$
 (A.28)

A.3. Market Product - Transmitter Coil Theory

The transmitter coil driving the market product will have a rectangular shape, as illustrated in Figure A.3.

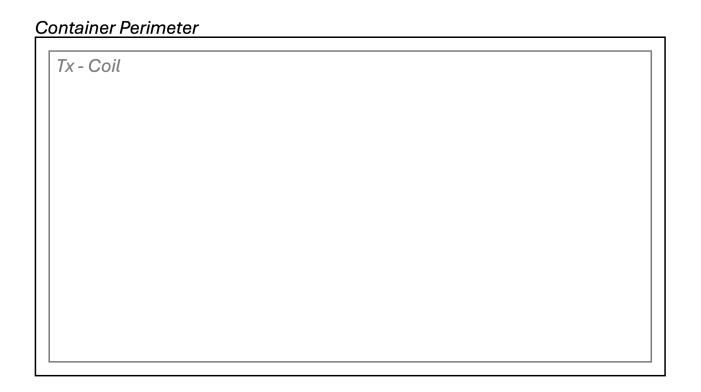


Figure A.3: Schematic illustration of the container ceiling featuring the rectangular-shaped transmitter coil.

However, as mentioned in 4.2, to analyse and design a functional market product, the rectangular transmitter will be approximated using two identical circular coils, as illustrated in Figure A.4.

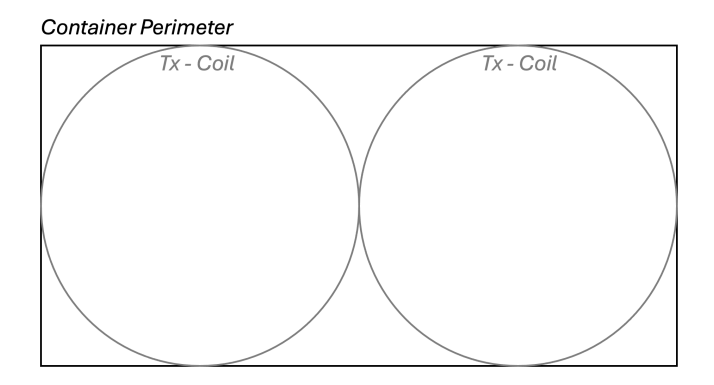


Figure A.4: Schematic illustration of the approximation of the transmitter coil.

Transmitter Coil Inductance

Due to the container's shape and size, a rectangular coil is the most suitable conductor for the transmitter. However, the inductance approximation given by Eq. 3.9 does not apply to rectangular inductances. Instead, the approximation, noted by Eq. A.29, provided by [20] for a rectangular loop offers a reliable estimate of the self-inductance for such a coil.

$$L_{\text{loop}} = \frac{\mu_0}{\pi} \left[-l \ln \left(1 + \sqrt{1 + \left(\frac{w}{l} \right)^2} \right) - w \ln \left(1 + \sqrt{1 + \left(\frac{l}{w} \right)^2} \right) + l \ln \left(\frac{2w}{r_w} \right) + w \ln \left(\frac{2l}{r_w} \right) + 2\sqrt{l^2 + w^2} - 2w - 2l \right], \quad l, w \gg r_w$$
 (A.29)

In this equation, r_w , l, and w represent the wire thickness, length, and width of the inductor, respectively. Due to the large container dimensions, a single loop is sufficient. As stated in the Programme of Requirements, a typical container measures 6 by 2.4 meters. Substituting these values, and using a common wire thickness (such as 1 mm) to reduce production costs, yields the following self-inductance:

$$\begin{split} L_{\text{loop}} &= \frac{4\pi \times 10^{-7}}{\pi} \bigg[- 6 \ln \left(1 + \sqrt{1 + \left(\frac{2.4}{6} \right)^2} \right) - 2.4 \ln \left(1 + \sqrt{1 + \left(\frac{6}{2.4} \right)^2} \right) \\ &+ 6 \ln \left(\frac{2 \times 2.4}{0.001} \right) + 2.4 \ln \left(\frac{2 \times 6}{0.001} \right) + 2\sqrt{6^2 + 2.4^2} - 2 \times 2.4 - 2 \times 6 \bigg] \approx 24.8 \ \mu\text{H} \end{split}$$

Where a resonance capacitor value, calculated with 3.16, of 0.77 µF is necessary to resonate with the source.



Appendix B - Simulations and Measurements

B.1. Simulations and Measurements

B.1.1. Prototype Measurements and Simulations

Figure B.1 presents the simulated LTspice circuit along with a sample simulation at a distance of d = 1 m.

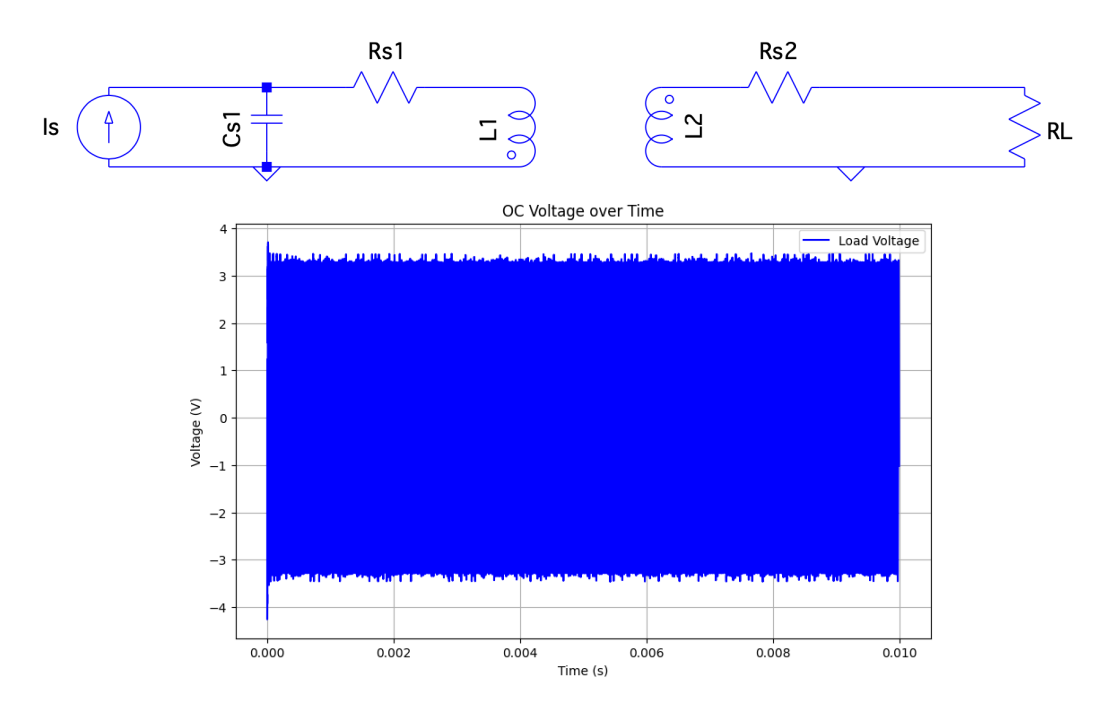


Figure B.1: The simulated schematic of the uncompensated energy harvesting circuit is shown at the top, while the sample voltage at d = 1 m is displayed at the bottom. In the schematic, the component values match those listed in Table 4.1. The source current was set to 1 A at 36.48 kHz, and the load resistance was chosen to be 5 M Ω .

B.1.2. Additional PCE simulations.

The SPICE model for the PMEG10010ELR shottky diode includes most of the relevant non-idealities such as junction capacitance, series resistance and reverse leakage. As such the simulations assessing PCE of pre- and post boost rectifier combinations were conducted in LTSpice using the aforementioned diode model attached to a fixed (ideal) 10μ F capacitor and $1M\Omega$ load. Since the PCE is input-dependent, simulations were conducted between input voltage amplitudes of 0.2V - 7V in 100mV increments.

Given that the full-bridge rectifiers and charge pumps obtain a higher power conversion efficiency at high input voltages (as shown in figure 3.12), a pre-boosting step-up transformer seems like the logical choice. Pre-rectification voltage boosting was briefly attempted by means of self-wound step-up transformers, but under-performed compared to simulations. Due to the limited project time implementation of a step-up transformer could not be realized.

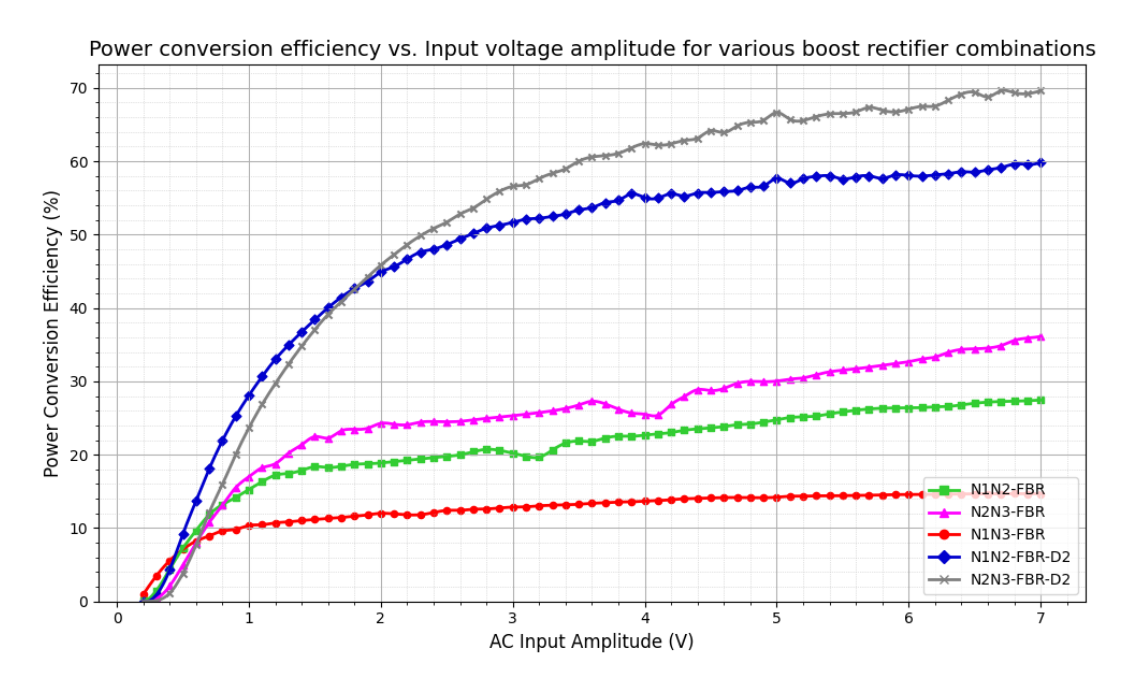


Figure B.2: Simulated PCE of various pre-post- and hybrid-boosting topologies using LTspice. NXNY denoting winding ratio (X:Y) of pre-rectification step-up transformer, D2 denoting 2 diode charge-pump.

B.1.3. Additional simulations of the complete system

Seen below is a comparisson of the complete system's output voltage over distance for the market product Tx-coil as presented in section 4.2, for FBR using the PMEG10010ELR and BAT54 shottky diodes.

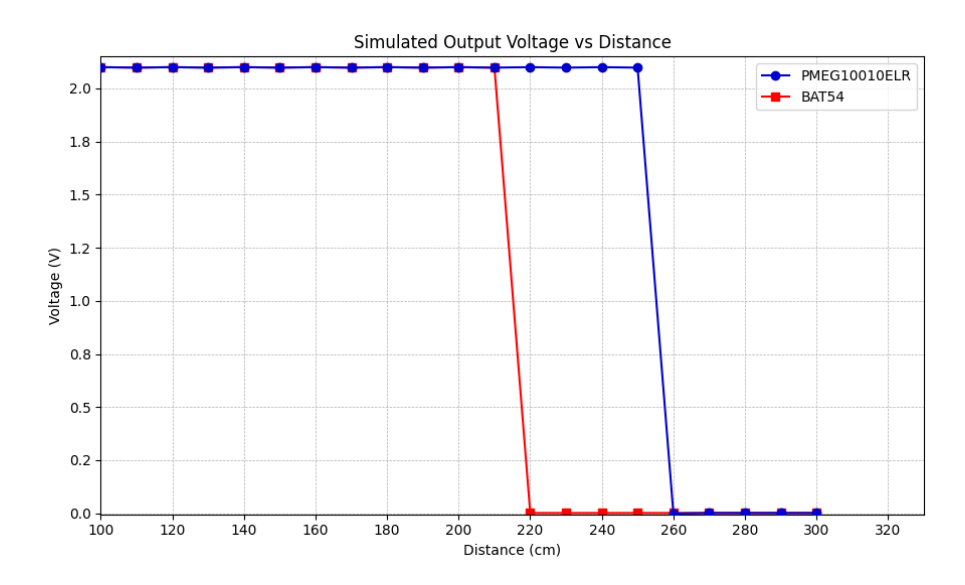


Figure B.3: Simulated DC output voltage (as seen at the output of the buck-boost) over distance for PMEG10010ELR and BAT54 based FBRs using LTspice.

Note that although the BAT54 achieves a higher PCE than the PMEG10010ELR at sub-volt inputs, the sys-

tem's cold-start range is superior for the PMEG10010ELR, likely due to the fact that the LTC3129 cannot start at voltages below 1 volt. At voltages above 2 volt, where LTC3129 start-up is possible, the PMEG10010ELR significantly outperforms the BAT54 in terms of PCE, as shown in figure 3.10, this could be the reason for the PMEG10010ELR's improved performance observed in simulations.

B.2. Measurement setup and assembled prototype

Figure B.4 presents the measurement setup used to determine the open-circuit voltage as a function of distance, featuring both a schematic representation and an actual image of the setup.

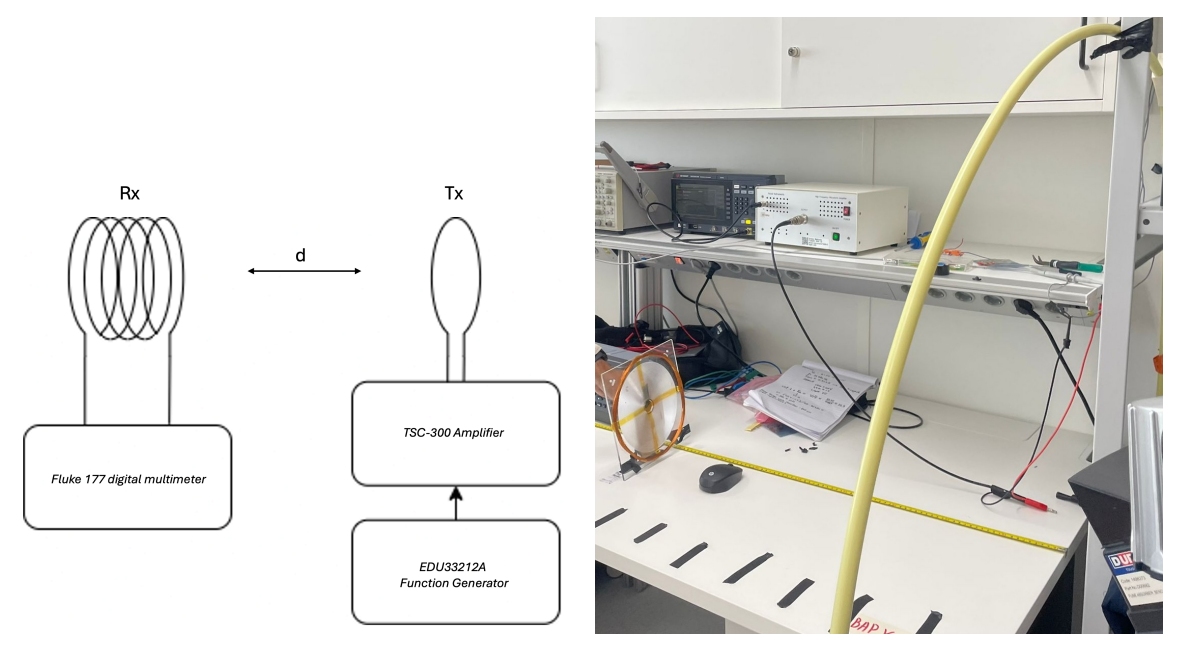


Figure B.4: On the left, a schematic illustrates the measurement setup used to determine the open-circuit voltage at the terminals of the receive coil as the distance increases. On the right, an image displays the actual setup.

After testing the prototype at various stages using a breadboard, the final version was soldered onto a perf board and made ready for use. Figure B.5 presents an image of the completed soldered prototype.

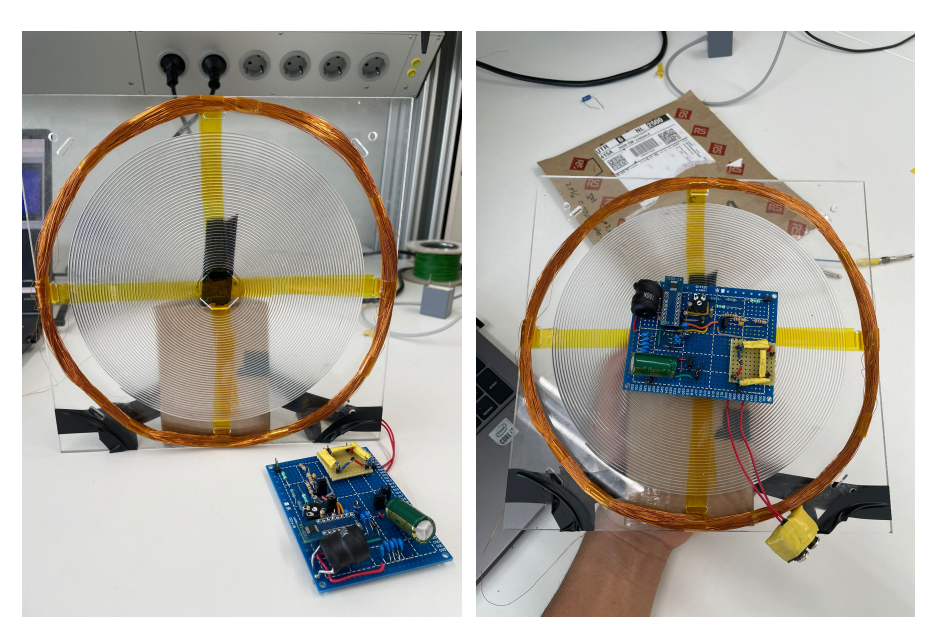


Figure B.5: The assembled prototype, without a case.



Appendix C - Code

C.1. Impedance Analyser Readings

Coil 1 data: SPOEL1.CSVCoil 2 data: SPOEL2.CSV

Code used for Plotting

```
import matplotlib.pyplot as plt
import numpy as np
def read impedance data(filename):
    """Reads impedance data from Keysight CSV file"""
   frequencies = []
   impedance = []
   read_data = False
   with open(filename, 'r') as f:
       for line in f:
            line = line.strip()
            if line.startswith('BEGIN CH1 DATA'):
                read data = True
                next(f) # Skip header line
                continue
            if read_data and line and not line.startswith('!'):
                parts = line.split(',')
                if len(parts) == 2:
                    try:
                        freq = float(parts[0])
                        z = float(parts[1])
                        frequencies.append(freq)
                        impedance.append(z)
                    except ValueError:
                        continue
   return np.array(frequencies), np.array(impedance)
# Read data from both files
freq1, z1 = read_impedance_data('SPOEL1.CSV')
freq2, z2 = read_impedance_data('SPOEL2.CSV')
# Find peak values
```

```
peak idx1 = np.argmax(z1)
peak idx2 = np.argmax(z2)
peak_freq1, peak_z1 = freq1[peak_idx1], z1[peak_idx1]
peak freq2, peak z2 = freq2[peak idx2], z2[peak idx2]
# Create plot
plt.figure(figsize=(12, 6))
plt.semilogx(freq1, z1, label=f'SPOEL1 (Peak: {peak z1:.2f} \Omega @ {peak freq1:.2f}
plt.semilogx(freq2, z2, label=f'SPOEL2 (Peak: {peak z2:.2f} \Omega @ {peak freq2:.2f}

   Hz) ')

# Formatting
plt.title('Impedance vs Frequency', fontsize=14)
plt.xlabel('Frequency (Hz)', fontsize=12)
plt.ylabel('|Z| (Ohm)', fontsize=12)
plt.legend(loc='upper left', fontsize=10)
plt.grid(True, which='both', linestyle='--', alpha=0.6)
plt.tight layout()
# Show plot
plt.show()
```

C.2. OC Voltage vs Distance Plots

C.2.1. LT-spice Simulation Results

```
import matplotlib.pyplot as plt
import numpy as np
from scipy.optimize import curve_fit
# LT-spice data points
d = np.array([0, 10, 20, 30, 40, 50, 60, 70, 80, 90, 100, 110, 120, 130, 140])
→ Distance in cm
V OC = np.array([18.6, 18.0, 16.5, 14.4, 11.9, 9.7, 7.8, 6.3, 5.0, 4.0, 3.2, 2.6,
 → 2.2, 1.8, 1.5]) # Open-circuit voltage in V
# Define an exponential decay function for fitting
def exp_decay(x, a, b):
   return a * np.exp(-b * x)
# Fit the exponential decay trendline
params, _ = curve_fit(exp_decay, d, V_OC, p0=[20, 0.05]) # Initial guesses for
 → parameters
# Generate trendline predictions
d_future = np.linspace(0, 180, 100) # Extend distance for future predictions
V_OC_future = exp_decay(d_future, *params)
# Plot data points
plt.figure(figsize=(10, 6))
plt.scatter(d, V OC, color='blue', label="Measured Data", zorder=3)
plt.plot(d future, V OC future, color='red', linestyle='dashed', label="Exponential
→ Trendline", zorder=2)
# Labels and title
plt.xlabel("Distance (cm)")
plt.ylabel("Open Circuit Voltage (V)")
plt.title("Voltage vs. Distance according to LT-spice Simulations")
plt.legend()
plt.grid(True)
```

```
# Show plot
plt.show()
```

C.2.2. Measurement Results

```
import matplotlib.pyplot as plt
import numpy as np
from scipy.optimize import curve fit
# Measured data points
d = np.array([0, 10, 20, 30, 40, 50, 60, 70, 80, 90, 100, 110, 120, 130, 140]) #
→ Distance in cm
V OC = np.array([20.996, 16.734, 14.174, 10.796, 8.231, 6.640, 5.153, 4.470, 3.543,
 4 2.707, 2.201, 1.826, 1.389, 1.128, 0.824]) # Open-circuit voltage in V
# Define an exponential decay function for fitting
def exp_decay(x, a, b):
    return a * np.exp(-b * x)
# Fit the exponential decay trendline
params, _ = curve_fit(exp_decay, d, V_OC, p0=[20, 0.05]) # Initial guesses for
 → parameters
# Generate trendline predictions
d_future = np.linspace(0, 180, 100) # Extend distance for future predictions
V_OC_future = exp_decay(d_future, *params)
# Plot data points
plt.figure(figsize=(10, 6))
plt.scatter(d, V OC, color='blue', label="Measured Data", zorder=3)
plt.plot(d future, V OC future, color='red', linestyle='dashed', label="Exponential

    Trendline", zorder=2)

# Labels and title
plt.xlabel("Distance (cm)")
plt.ylabel("Open Circuit Voltage (V)")
plt.title("Measured Voltage vs. Distance")
plt.legend()
plt.grid(True)
# Show plot
plt.show()
```

C.3. Rectification, Protection and Output Stabilization Measurements

```
return np.piecewise(
        [x <= 60, x > 60],
        [lambda x: a, lambda x: b * np.exp(-c * (x - 60))]
    )
# Fit only the exponential part (after 60 cm)
initial guess = [2.1, 2.1, 0.05]
popt, _ = curve_fit(piecewise_model, distances_sorted, voltages sorted,

   p0=initial guess)

# Generate smooth x values and compute fitted y values
x = np.linspace(0, 180, 500)
y_smooth = piecewise_model(x_smooth, *popt)
# Plotting
plt.figure(figsize=(10, 6))
plt.plot(distances sorted, voltages sorted, 'o-', label='Measured Voltages',
⇔ color='blue')
plt.plot(x smooth, y smooth, '--', label='Trendline', color='purple')
plt.xlabel('Distance (cm)')
plt.ylabel('Voltage (V)')
plt.title('Voltage vs Distance')
plt.xlim(0, 180)
plt.grid(True)
plt.legend()
plt.tight_layout()
plt.show()
```

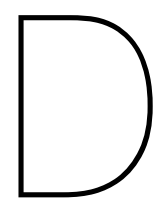
C.4. Complete system SPICE Netlist

```
*Market Tx version
R2 N006 AC+ 0.05
R3 out N007 125
I1 0 AC+ SINE(0 3 50000)
L1 N006 0 456.3D
L2 N007 N010 55m
C1 0 N008 5 Rser=0.1
D1 out N008 PMEG10010ELR
D2 N010 N008 PMEG10010ELR
D3 0 N010 PMEG10010ELR
D4 0 out PMEG10010ELR
D5 0 N008 BZX79C13
L3 N002 N001 100 Rser=20m
C2 N002 N004 6.8n
C3 N003 N005 6.8n
R1 DC OUT N009 6.2Meg
XU1 0 N004 N002 MP_01 N008 N008 N011 N011 N009 N005 0 N003 NC 02 DC OUT LTC3129
R4 0 N009 8Meg
C4 N011 0 10 Rser=5
Cb1 DC OUT 0 10
R5 N001 N003 8.8m
I mcul DC OUT 0 1.10
.model D D
.lib C:\Users\Documents\LTspiceXVII\lib\cmp\standard.dio
* PCE calculation:
.meas P in AVG -I(V1)*V(AC+,AC-) FROM 0.3 TO 0.5
.meas P out AVG (I(R1)*V(inbb)) FROM 0.3 TO 0.5
.meas PCE1 AVG (P out/P in) *100 FROM 0.3 TO 0.5
* Input sweep:
* .step param VinAmp 0.2 7 0.1
```

```
.meas V_out MAX V(out)
* average DC output:
.MODEL BZX79C13 D IS= 2.524e-016 RS= 0.5164 CJO= 1e-012 VJ= 0.75
+ TT= 5e-009 M= 0.3333 BV= 13.1 IBV= 0.2655 N= 1
+ EG= 1.11 XTI= 3 KF= 0 AF= 1 FC= 0.5
+ TNOM= 27
.meas Irms RMS I(V1)
.step param K1 list 0.00484716, 0.00479710, 0.00465198, 0.00442582, 0.00413858,

    0.00381242, 0.00346834, 0.00312388, 0.00279213, 0.00248174, 0.00219759,
    0.00194161, 0.00171373, 0.00151257, 0.00133602, 0.00118166, 0.00104699,

 4 0.00092961, 0.00082730, 0.00073806, 0.00066013, 0.00059197, 0.00053222,
 4 0.00047974, 0.00043354, 0.00039277, 0.00035671, 0.00032472, 0.00029628,
 o.00027094, 0.00024830
K L1 L2 {K1}
.lib LTC3129.sub
.backanno
.end
```



Appendix D - List of Used Components

D.1. List of Components

To construct the prototype/ demonstrator, the following components were used:

- · Coil materials:
 - 32 AWG enamelled copper wire: ±180 meters.
 - Acrylic sheet: 15 x 15 cm
- · Components and ammount used:
 - PMEG10010ELR Schottky diodes: 4
 - LTC3129 Buck-boost converter: 1
 - FG1414X7R1A106KRT00 10 μ F X7R Ceramic Capacitors: 8
 - Chanxin VENT 3300 μF Electrolytic Capacitor: 1
 - Phillips 22 μ F 25 V 030K0 Electrolytic Capacitor: 1
 - DIP 10 µH Coil inductor: 1
 - BZX79C13 Zener diode: 1

D.2. Temperature Details

Table D.1 presents the temperature tolerance ranges of the components used in the prototype's construction, as well as those intended for the market product. The data confirms that both the prototype and the market product operate within the temperature range required by the PoR.

| Component | Minimum Temperature [°C] | Maximum Temperature [°C] |
|--|--------------------------|--------------------------|
| Coils (Tx & Rx) | -40 | +85 |
| LTC3129 Buck-boost converter | -40 | +125 |
| PMEG10010ELR Schottky diode | – 55 | +175 |
| FG1414X7R1A106KRT00 10 µF X7R Ceramic Capacitor | – 55 | +125 |
| Chanxin VENT 3300 µF Electrolytic Capacitor | -40 | +105 |
| Phillips 22 µF 25 V 030K0 Electrolytic Capacitor | -40 | +105 |
| DIP 10 µH Coil inductor | -40 | +85 |
| BZX79C13 Zener diode | – 65 | +200 |

Table D.1: Operating temperature ranges for components based on datasheets and material properties.

D.3. Specifications of Used Capacitors

| Part Name | Capacitance | ESR | Self-Discharge Resistance |
|--------------------------------|-------------|---------------------------------|---|
| FG1414X7R1A106KRT100 | 10μF | <100 m Ω (typical) | 10^9 - 10^{12} M Ω (typical) |
| Changxin VENT 3300 25V μ F | 3300μF | 10-100 m Ω (approximate) | 1-10 M Ω (approximate) |
| Phillips 25 V 030K0 | 22 μF | 10 Ω (typical) | 1-10 M Ω (approximate) |

Table D.2: Capacitor Specifications

Bibliography

- [1] International Telecommunication Union (ITU). *E-Waste Recycling: Global Progress and Challenges*. https://www.itu.int/en/mediacentre/Pages/PR-2024-03-20-e-waste-recycling.aspx. 2024.
- [2] United Nations University (UNU). Global E-Waste Surging: 21% Increase Over 5 Years. https://unu.edu/press-release/global-e-waste-surging-21-5-years. 2024.
- [3] A. Reunis and K. de Wit. *Ultra Low Power Sensor Readout and Data Logger*. Delft, The Netherlands, 2025.
- [4] Accel Instruments. TS250 Waveform Amplifier Datasheet. https://www.accelinstruments.com/Products/TS250/Waveform-Amplifier.pdf. 2025.
- [5] Y. P. Tian et al. "Design and Analysis of RF Energy Harvesting Systems". In: *IEEE Transactions on Microwave Theory and Techniques* 57.8 (2009), pp. 2000–2007.
- [6] Charles K. Alexander and Matthew N. O. Sadiku. *Fundamentals of Electric Circuits*. McGraw Hill, 2021, pp. 1754–1765, 1710–1729, 759, 71–80. ISBN: 978-1-260-57079-3.
- [7] R. Badia-Melis et al. "New trends in cold chain monitoring applications A review". In: Food Control 86 (2018), pp. 170-182. ISSN: 0956-7135. DOI: https://doi.org/10.1016/j.foodcont.2017.11.022. URL: https://www.sciencedirect.com/science/article/pii/S0956713517305558.
- [8] University of Central Florida. *Magnetic Field of a Current Loop*. https://pressbooks.online.ucf.edu/osuniversityphysics2/chapter/magnetic-field-of-a-current-loop/. 2025.
- [9] Thomas Roy Crompton. Battery reference book. Newnes, 2000.
- [10] M. Haerinia and R. Shadid. "Wireless Power Transfer Approaches for Medical Implants: A Review". In: Signals 1.2 (2020), pp. 209–229. DOI: https://doi.org/10.3390/signals1020012. URL: https://www.mdpi.com/2504-4494/1/2/12.
- [11] H. H. Ibrahim et al. "Radio Frequency Energy Harvesting Technologies: A Comprehensive Review on Designing, Methodologies, and Potential Applications". In: Sensors 22.11 (2022), p. 4144. DOI: 10.3390/s22114144.
- [12] Keysight Technologies. EDU33210 Series 20 MHz Function/Arbitrary Waveform Generators Datasheet. https://www.keysight.com/us/en/assets/3121-1004/data-sheets/EDU33210-Series-20-MHz-Function-Arbitrary-Waveform-Generators.pdf. 2025.
- [13] Koji Kotani, Atsushi Sasaki, and Takashi Ito. "High-Efficiency Differential-Drive CMOS Rectifier for UHF RFIDs". In: *IEEE Journal of Solid-State Circuits* 44.11 (2009), pp. 3011–3018. DOI: 10.1109/JSSC.2009.2028955.
- [14] A. Kurs et al. "Wireless Power Transfer via Strongly Coupled Magnetic Resonances". In: *Science* 317.5834 (2007), pp. 83–86.
- [15] Linear Technology. 15V, 200mA Synchronous Buck-Boost DC/DC Converter with 1.3µA Quiescent Current Data sheet. https://www.analog.com/media/en/technical-documentation/data-sheets/3129fc.pdf. 2015.
- [16] Nexperia. BAT54 Schottky Barrier Diode Datasheet. https://assets.nexperia.com/documents/data-sheet/BAT54.pdf. Accessed: 2024-06-06. 2022.
- [17] Nexperia. BZX79-Voltage regulator diodes. https://assets.nexperia.com/documents/data-sheet/BZX79.pdf. 2002.

- [18] Nexperia. PMEG10010ELR: 100 V, 1 A Low Leakage Current Schottky Barrier Rectifier Datasheet. https://www.nexperia.com/products/diodes/schottky-diodes/schottky-rectifiers/PMEG10010ELR.html. Accessed: 2024-06-06. 2023.
- [19] J. Paradiso and T. Starner. "Energy Scavenging for Mobile and Wireless Electronics". In: *IEEE Pervasive Computing* 4.1 (2005), pp. 18–27. DOI: 10.1109/mprv.2005.9.
- [20] Clayton R. Paul. Inductance: Loop and Partial. Wiley-IEEE Press, 2009. Chap. 4.
- [21] Dalibor Purkovic. "Supercapacitors as Guarantors for Energy Sustainability in Low-Power Energy Harvesting Sensor Modules". In: *Exergy and Its Application*. Ed. by Muhammad Aziz. Rijeka: IntechOpen, 2019. Chap. 5. DOI: 10.5772/intechopen.88007. URL: https://doi.org/10.5772/intechopen.88007.
- [22] "10 Diode Rectifiers". In: Power Electronics Handbook (Third Edition). Ed. by Muhammad H. Rashid. Third Edition. Boston: Butterworth-Heinemann, 2011, pp. 149–181. ISBN: 978-0-12-382036-5. DOI: https://doi.org/10.1016/B978-0-12-382036-5.00010-0. URL: https://www.sciencedirect.com/science/article/pii/B9780123820365000100.
- [23] Umberto Ravaioli and Fawwaz Tayssir Ulaby. *Fundamentals of Applied Electromagnetics*. Pearson, 2022, pp. 252, 289–301.
- [24] E. B. Rosa and F. W. Grover. "Formulas for Mutual and Self-Inductance". In: *Bulletin of the Bureau of Standards* 8.1 (1911), pp. 1–233. URL: https://nvlpubs.nist.gov/nistpubs/bulletin/08/nbsbulletinv8n1p1 A2b.pdf.
- [25] D. M. Rowe. "Thermoelectrics, an environmentally friendly source of electrical power". In: *Renewable Energy* 16.1–4 (1999), pp. 1251–1256.
- [26] S. Dinev and B. Joemmankhan. *Wireless RF transmission for a batteryless temperature logger*. Delft, The Netherlands, 2025.
- [27] European Agency for Safety and Health at Work (OSHA). Guidelines on Council Recommendation 1999/519/EC for Limiting Exposure to Electromagnetic Fields. https://osha.europa.eu/en/legislation/guidelines/council-recommendation-1999519ec-limitation-exposure-general-public-electromagnetic-fields-0-hz-300-ghz. 2025.
- [28] R.L. Spyker and R.M. Nelms. "Classical equivalent circuit parameters for a double-layer capacitor". In: *IEEE Transactions on Aerospace and Electronic Systems* 36.3 (2000), pp. 829–836. DOI: 10.1109/7.869502.
- [29] Michael Steer. Microwave and RF Design III Networks. LibreTexts Engineering, 2025. URL: https://eng.libretexts.org/Bookshelves/Electrical_Engineering/Electronics/Microwave_and_RF_Design_III_-_Networks_%28Steer%29/06%3A_Chapter_6/6.4%3A_The_L_Matching_Network.
- [30] Yen Kheng Tan. Energy Harvesting Autonomous Sensor Systems: Design, Analysis, and Practical Implementation. CRC Press, 2013.
- [31] Toru Tanzawa. *Design of DC-DC switched-capacitor voltage multiplier driven by DC energy transducer.* **2014**. **DOI**: 10.1109/ICECS.2014.7049988.
- [32] TU Delft. Structured Electronics Design Analog Electronics. https://analog-electronics.tudelft.nl/. 2025.
- [33] Fred G. Turnbull and Ondrej Pauk. 14 Power Electronics—Rectifiers, Filters, and Power Supplies. Ed. by Wendy M. Middleton and Mac E. Van Valkenburg. Ninth Edition. Woburn: Newnes, 2002, pp. 14-1-14-51. ISBN: 978-0-7506-7291-7. DOI: https://doi.org/10.1016/B978-075067291-7/50016-9. URL: https://www.sciencedirect.com/science/article/pii/B9780750672917500169.
- [34] European Union. Council Recommendation 1999/519/EC: Limitation of Exposure of the General Public to Electromagnetic Fields (0 Hz to 300 GHz). https://eur-lex.europa.eu/eli/reco/1999/519/oj/eng. 1999.
- [35] UNITAR. Global E-Waste Monitor 2024: Electronic Waste Rising Five Times Faster than Documented E-Waste Recycling. https://unitar.org/about/news-stories/press/global-e-waste-monitor-2024-electronic-waste-rising-five-times-faster-documented-e-waste-recycling. 2024.

- [36] Davor Vinko. "Applicability of Dickson charge pump in energy harvesting systems: Experimental validation of energy harvesting charge pump model". In: *Radioengineering* 27.2 (2018), p. 511.
- [37] Jason Lee Wardlaw and Aydın İlker Karsilayan. "Self-Powered Rectifier for Energy Harvesting Applications". In: *IEEE Journal on Emerging and Selected Topics in Circuits and Systems* 1.3 (2011), pp. 308–320. DOI: 10.1109/JETCAS.2011.2164975.
- [38] X. Wei, Z. Wang, and H. Dai. "A Critical Review of Wireless Power Transfer via Strongly Coupled Magnetic Resonances". In: *Energies* 7.7 (2014), pp. 4316–4341. DOI: https://doi.org/10.3390/en7074316. URL: https://www.mdpi.com/1996-1073/7/7/4316.
- [39] S. W. Wright et al. "Inductive Energy Harvesting From Current-Carrying Structures". In: *IEEE Sensors Letters* **3.6** (June 2019), pp. 1–4. DOI: 10.1109/LSENS.2019.2918339.
- [40] Lei Zhang et al. "A review of supercapacitor modeling, estimation, and applications: A control/management perspective". In: Renewable and Sustainable Energy Reviews 81 (2018), pp. 1868—1878. ISSN: 1364-0321. DOI: https://doi.org/10.1016/j.rser.2017.05.283. URL: https://www.sciencedirect.com/science/article/pii/S1364032117309292.